Highlights of Joint Research

Supercomputer Center

The Supercomputer Center (SCC) is a part of the Materials Design and Characterization Laboratory (MDCL) of ISSP. Its mission is to serve the whole community of computational condensed-matter physics of Japan providing it with high performance computing environment. In particular, the SCC selectively promotes and supports large-scale computations. For this purpose, the SCC invites proposals for supercomputer-aided research projects and hosts the Steering Committee, as mentioned below, that evaluates the proposals.

The ISSP supercomputer system consists of three subsystems: System A, which is intended for a parallel computation with relatively smaller number of nodes connected tightly, and System B, which is intended for more nodes with relatively loose connections. In July, 2010, the SCC replaced the two supercomputer subsystems. The current system B is SGI Altix ICE 8400EX, which consists of 30 racks or 15360 cores whereas the system A is NEC SX-9, which consists of 4 nodes or 64 cpus. They have totally 200 TFlops. System C - FUJITSU PRIMEHPC FX10 was installed in April, 2013. It is highly compatible with K computer, the largest supercomputer in Japan. System C consists of 384 nodes, and each node has 1 SPARC64TM IXfx CPU (16 cores) and 32 GB of memory. The total system achieves 90.8 TFlops theoretical peak performance.

The hardware administration is not the only function of the SCC. The ISSP started hosting Computational Materials Science Initiative (CMSI), a new activity of promoting materials science study with next-generation parallel supercomputing. This activity is financially supported by the MEXT HPCI strategic program, and in CMSI, a number of major Japanese research institutes in various branches of materials science are involved. The SCC supports the activities of CMSI as its major mission.

All staff members of university faculties or public research institutes in Japan are invited to propose research projects (called User Program). The proposals are evaluated by the Steering Committee of SCC. Pre-reviewing is done by the Supercomputer Project Advisory Committee. In school year 2014 totally 247 projects were approved. The total points applied and approved are listed on Table. 1 below.

The research projects are roughly classified into the following three (the number of projects approved):

First-Principles Calculation of Materials Properties (119)
Strongly Correlated Quantum Systems (38)
Cooperative Phenomena in Complex, Macroscopic Systems (90)

All the three involve both methodology of computation and its applications. The results of the projects are reported in 'Activity Report 2014' of the SCC. Every year 3-4 projects are selected for "invited papers" and published at the beginning of the Activity Report. In the Activity Report 2014, the following three invited papers are included:

"All-Electron First-Principles GW+Bethe-Salpeter Program: Development & Applications", Yoshifumi NOGUCHI
"First-Principles Study on Superconductivity in Alkali-Doped Fullerides", Ryotaro ARITA
"Development of Simulation Methods for Membrane Protein Structure Predictions and Replica-Exchange Methods", Ryo URANO and Yuko OKAMOTO

Class	Max/Min Points	Application	Number of Projects	Total Points					
				Applied			Approved		
				System A	System B	System C	System A	System B	System C
A	100	any time	9	500	600	400	500	600	400
B	2k, 1k, 500	twice a year	53	40.8k	44.8k	6.3k	33.8k	29.4k	5.7k
C	20k, 10k, 2.5k	twice a year	151	637.0k	1210.2k	141.2k	429.0k	360.5k	111.4k
D	20k, 10k, 2.5k	any time	10	12.0k	71.7k	0	12.0k	57.6k	0
E	0, 30k, 2.5k	twice a year	23	-	621.0k	42.0k	-	270.0k	37.4k
S		twice a year	1	0	60.0k	0	0	25.0k	0
CMSI			18	-	-	-	-	-	140.0k
Total			265	690.3k	2,008.3k	189.9k	475.3k	743.1k	294.9k

Table 1. Research projects approved in 2014
The maximum points allotted to the project of each class are the sum of the points for the two systems; Computation for 1 CPU· hour corresponds to 0.32, 0.022, and 0.042 points for System-A, System-B, and System C, respectively.

Neutron Science Laboratory

The Neutron Science Laboratory (NSL) has been playing a central role in neutron scattering activities in Japan since 1961 by performing its own research programs as well as providing a strong General User Program for the university-owned various neutron scattering spectrometers installed at the JRR-3 (20MW) operated by Japan Atomic Energy Agency (JAEA) in Tokai (Fig. 1). In 2003, the Neutron Scattering Laboratory was reorganized as the Neutron Science Laboratory to further promote the neutron science with use of the instruments in JRR-3. Under the General User Program supported by NSL, 14 university-group-owned spectrometers in the JRR-3 reactor are available for a wide scope of researches on material science, and proposals close to 300 are submitted each year, and the number of visiting users under this program reaches over 6000 person-day/year. In 2009, NSL and Neutron Science Laboratory (KENS), High Energy Accelerator Research Organization (KEK) built a chopper spectrometer, High Resolution Chopper Spectrometer, HRC, at the beam line BL12 of MLF/J-PARC (Materials and Life Science Experimental Facility, J-PARC). HRC covers a wide energy and Q-range ($10\mu eV < \hbar\omega < 2eV$ and $0.02\text{Å}^{-1} < Q < 50\text{Å}^{-1}$), and therefore becomes complementary to the existing inelastic spectrometers at JRR-3. HRC started to accept general users through the J-PARC proposal system in FY2011.

Triple axis spectrometers, chopper spectrometer (HRC), and a high resolution powder diffractometer are utilized for a conventional solid state physics and a variety of research fields on hard-condensed matter, while in the field of soft-condensed matter science, researches are mostly carried out by using the small angle neutron scattering (SANS-U) and/or neutron spin echo (iNSE) instruments. The upgraded time-of-flight (TOF) inelastic scattering spectrometer, AGNES, is also available through the ISSP-NSL user program.

On March 11, 2011, a great earthquake with Magnitude 9.0 hit North East Coast of Japan. Fortunately, JRR-3 was under regular inspection and no serious accidents or damages were reported. However, the lifeline of Tokai Village area was lost for more than two weeks, and it took more than two months before damage inspection of JRR-3 could be started. As of May of 2015, JRR-3 has not restarted yet. General User Programs of 2011 - 2014 were cancelled and that of 2015 has been suspended so far. In order to compensate the

Fig. 2. The U.S.-Japan spectrometer, CTAX, installed at the cold guide-line CG4, High Flux Isotope Reactor (HFIR), in Oak Ridge National Laboratory. Members who contributed the relocation project of the U.S.-Japan spectrometer celebrate the completion of the project in October 2010.)

loss of the activity of NSL, a number of proposals accepted in 2011 - 2014 were transferred to overseas owing to kind offer from the major facilities, namely, ORNL, ILL, ANSTO, and HANARO.

Research topics in FY2013 cover Hydrogen release from Li alanates originates in molecular lattice instability (6G:TOPAN T1-3:HERMES), Direct observation of antiferromagnetic ordering in s electrons confined in regular nanospace of sodalite (5G:PONTA), SANS Studies on Catalyst Ink of Fuel Cell (SANS-U), Neutron scattering studies of Ti-Cr-V bcc alloy with the residual hydrogen and deuterium (AGNES). In addition, there are a variety of activities on fundamental physics, neutron beam optics, developments of neutron scattering techniques.

Progress of HRC spectrometer in FY2014 is the development of the magnetic field environment. We examined a performance test of a superconducting magnet on the HRC goniometer. The magnetic field of 10 T was achieved with normal operation of the related components in the straying field. The magnitude of the field is the highest record in J-PARC/MLF at present. By using radial collimator for the reduction of background scattering from Aluminum supporting ring in the magnet, high-quality data was collected. The magnet is now ready for the general user program.

The NSL also operates the U.S.-Japan Cooperative Program on neutron scattering, providing further research opportunities to material scientists who utilize the neutron scattering technique for their research interests. In 2010, relocation of the U.S.-Japan triple-axis spectrometer, CTAX, was completed, and it is now open to users (Fig. 2). http://neutrons.ornl.gov/instruments/HFIR/CG4C/

The activity report on Neutron Scattering Research in JFY2011 is given in NSL-ISSP Activity Report vol. 18 (2011), http://quasi.issp.u-tokyo.ac.jp/actrep/actrep-18-2011/index-pub_vol18.html.

Fig. 1. The reactor of JRR-3. The eight neutron scattering instruments are attached to the horizontal beam tubes in the reactor experimental hall. Two thermal and three cold guides are extracted from the reactor core towards the guide hall located to the left.

International MegaGauss Science Laboratory

The objective of this laboratory (Fig. 1) is to study the physical properties of solid-state materials (such as semiconductors, magnetic materials, metals, insulators, superconducting materials) under ultra-high magnetic field conditions. Such a high magnetic field is also used for controlling the new material phase and functions. Our pulse magnets, at moment, can generate up to 87 Tesla (T) by non-destructive manner, and from 100 T up to 760 T (the world strongest as an in-door record) by destructive methods. The laboratory is opened for scientists both from Japan and from overseas, especially from Asian countries, and many fruitful results are expected to come out not only from collaborative research but also from our in-house activities. One of our ultimate goals is to provide the scientific users as our joint research with magnets capable of a 100 T, milli-second long pulses in a non-destructive mode, and to offer versatile physical precision measurements. The available measuring techniques now involve magneto-optical measurements, cyclotron resonance, spin resonance, magnetization, and transport measurements. Recently, specific heat and calorimetric measurements are also possible to carry out with sufficiently high accuracy.

Our standard non-destructive-type pulse magnets are energized by single capacitor bank and can generate fields up to 75 T for ordinary use. Their simple sinusoidal waveforms are advantageous for precise and reliable measurements of various physical properties. Several on-demand magnets having irregular shapes and sizes are developed for some particular experiments. We open six magnet cells for parallel experiments and accept more than 50 research projects per year in 2013.

A 210 MJ flywheel generator (Fig. 2), which is the world largest DC power supply (recorded in the Guinness Book of World Records) has been installed in the DC flywheel generator station at our laboratory, and used as an energy source of long pulse magnets. The magnet technologies are intensively devoted to the quasi-steady long pulse magnet (an order of 1-10 sec) energized by the giant DC power supply. The latest long-pulse magnet can generate fields up to 36 T with its pulse half-period of 1 sec.

Our interests cover the study on quantum phase transitions (QPTs) induced by high magnetic fields. Field-induced QPTs have been explored in various materials such as quantum spin systems, strongly correlated electron systems and other magnetic materials. Direct thermodynamic evidences of QPTs are obtained through magnetization and recently developed caloric measurements. For some QPTs, changes in symmetry at the transitions are sensitively resolved through measurements of electric polarization or optical imaging using a polarizing microscope. High resolution of electrical measurements realized the observation of quantum oscillations in high quality crystals through measurements of electrical resistivity, contactless impedance, and torque magnetometry.

Magnetic fields higher than 100 T can only be obtained with destructing a magnet coil, where ultra-high magnetic fields are obtained in a microsecond time scale. Our destructive techniques have undergone intensive developments. The project, financed by the ministry of education, culture, sports, science and technology, is now in progress, and goal is to generate 1000 T by the electromagnetic flux compression (EMFC) system (Fig. 3). The system which is unique to ISSP in the world scale is comprised of a power source of 5 MJ main condenser bank and 2 MJ condenser bank and has been accomplished its installation. Two magnet stations are constructed and both are energized from each power source. Both systems are fed with a 2 MJ condenser bank used for a seed-field coil, of which magnetic flux is to be compressed.

As an easy access to the megagauss science and technology, we have the single-turn coil (STC) system capable of generating the fields of up to 300 T by a fast-capacitor of 200 kJ. We have two STC systems, one is a horizontal type (H-type) and the other is a vertical type (V-type, Fig. 4). Various kinds of laser spectroscopy experiments such as the cyclotron resonance and the Faraday rotation using the H-type STC are available. On the other hand, for very low-temperature experiments, a combination of the V-type STC with a liquid helium bath cryostat is very useful and the magnetization measurements at temperature as low as 2 K can be performed up to 120 T with high precision.

Fig. 2. The building for the flywheel generator (left hand side) and a long pulse magnet station (right hand side). The flywheel giant DC generator is 350 ton in weight and 5 m high (bottom). The generator, capable of a 51 MW output power with the energy storage 210 MJ, is planned to energize the long pulse magnet generating 100 T without destruction.

Fig. 1. Building view of the International MegaGauss Science Laboratory (C-building) at ISSP.

	Alias	Type	B_{max}	Pulse width Bore	Power source	Applications	Others
Building C Room 101-113	Electro- Magnetic Flux Compression	destructive	730 T	μs 10 mm	5 MJ, 40kV	Magneto-Optical Magnetization	5 K – Room temperature
	Horizontal Single-Turn Coil	destructive	300 T 200 T	μs 5 mm 10 mm	0.2 MJ, 50 kV	Magneto-Optical measurements Magnetization	5 K – 400 K
	Vertical Single-Turn Coil	destructive	300 T 200 T	μs 5 mm 10 mm	0.2 MJ, 40 kV	Magneto-Optical Magnetization	2 K – Room temperature
Building C Room 114-120	Mid-Pulse Magnet	Non-destructive	60 T 70 T	40 ms 18 mm 40 ms 10 mm	0.9 MJ, 10 kV	Magneto-Optical measurements Magnetization Magneto-Transport Hall resistance Polarization Magneto-Striction Magneto-Imaging Torque Magneto- Calorimetry Heat Capacity	Independent Experiment in 5 site Lowest temperature 0.1 K
Building C Room 121	PPMS	Steady State	14 T			Resistance Heat Capacity	Down to 0.3 K
	MPMS	Steady State	7 T			Magnetization	
Building K	Short-Pulse magnet	Non-destructive	87 T (2-stage pulse) 85 T	5 ms 10 mm 5 ms 18 mm	0.5 MJ, 20 kV	Magnetization Magneto-Transport	2K – Room temperature
	Long-Pulse magnet	Non-destructive	36 T	1 s 30 mm	210 MJ, 2.7 kV	Resistance Magneto-Calorimetry	2K – Room temperature

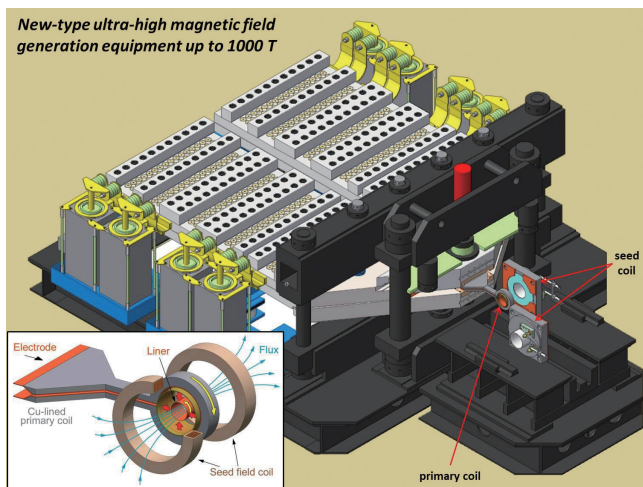Table 1. Available Pulse Magnets, Specifications

Fig. 3. (Build. C) The building for the electro-magnetic flux compression, generating over 700 T. 1000 T project started since 2010, and finally condenser banks of 9 MJ (5 MJ + 2 MJ +2 MJ) as a main system with the 2 MJ sub bank system for the seed field have been installed, and completed in the year of 2014.
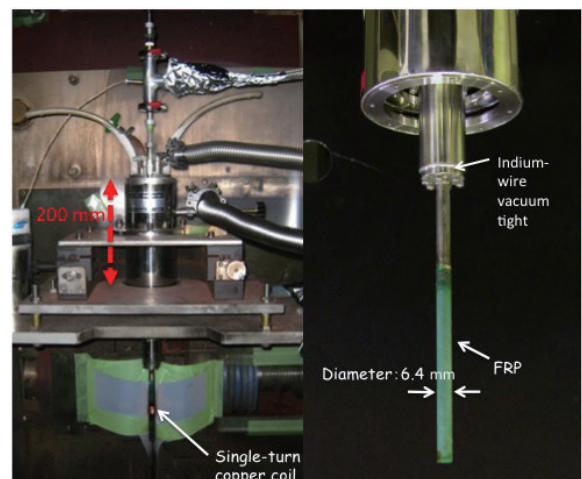

Fig. 4. Fig.4. A photo of the V-type single-turn coil equipped with 40 kV, (A:100+B:100=200 kJ) fast operating pulse power system. Measurements are carried out from room temperature down to 2 K by a specially designed cryostat.

Center of Computational Materials Science

With the advancement of hardware and software technologies, large-scale numerical calculations have been making important contributions to materials science and will have even greater impact on the field in the near future. Center of Computational Materials Science (CCMS) is a specialized research center for promoting computer-aided materials science with massively parallel computers, such as K-computer. The center also functions as the headquarters of Computational Materials Science Initiative (CMSI), which is an inter-institutional organization for computational science of a broad range of disciplines, including molecular science, quantum chemistry, biological materials, and solid state physics. ISSP made contracts with 9 universities and 2 national institutes for supporting the activities of CMSI in which nearly 100 research groups are involved. The main purpose of CMSI is to establish a new community of computational science in which researches from different backgrounds work together on grand challenge problems, thereby developing computational infrastructures (new algorithms, coding styles, standard software packages, etc) and inspire young scientists.

CCMS has a branch office in the RIKEN AICS building on the Port Island Kobe, where K-computer is located, for supporting CMSI researchers getting together at the K-computer site to exchange ideas of computational science, fine-tune various applications software for the K-computer, and develop better contact with staff members of RIKEN, the operating institute of K-computer. Another mission of the Kobe branch of CCMS is to communicate with researchers from other fields of computer science. (There are 5 major fields in the HPCI strategic program of MEXT, "biology", "materials and energy" (our field), "seismology, oceanography and meteorology", "industrial applications", and "high-energy physics and cosmology".)

The following is the selected list of meetings organized by CMSI and CCMS in SY2014:

- "CMSI Hands-On: FU Tutorial"
  (Apr 28, Aug 18/2014, Kobe)
- "CMSI Hands-On: Version Control System Tutorial"
  (May 30/2014, Kobe)
- "CMSI Hands-On: ALPS Tutorial"
  (June 16/2014, Kobe)
- "Workshop: Programming Techniques for K-Computer"
  (Jul 7-Jul 9/2014, Kobe)
- "CMSI Hands-On: AkaiKKR Tutorial"
  (June 30/2014, Kashiwa)
- "CMSI Division 1 Summer School"
  (Aug 18-Aug 22/2014, Biwako)
- "CMSI Hands-On: GPGPU Computing with OpenACC 2.0" (Aug 28/2014, Hongo)
- "Symposium: Collabration with National Experimental Facilities" (Sep. 02, Akihabara)
- "CMSI Hands-On: Rokko Tutorial"
  (Sep. 18/2014, Kobe)
- "Workshop: Possibilities of Post-K Computing"
  (Sep. 28, Tokyo)
- "CMSI Hands-On: OpenMX Tutorial"
  (Oct. 10/2014, Kobe)
- "CMSI Hands-On: ALPS Tutorial"
  (Oct. 16/2014, Kashiwa)
- "CMSI International Workshop 2014: Tensor Network Algorithms in Materials Science" (Oct. 20-22/2014, Kobe)
- "The 4th Symposium of CCMS"
  (Nov.12-14, Kashiwa)
- "10sor Network Workshop"
  (Nov. 25/2014, Kashiwa)
- "The 5th CMSI Symposium"
  (Dec.08-10/2014, Sendai)
- "CMSI Hands-On: xTAPP Tutorial"
  (Dec. 12/2014, Kashiwa)
- "CMSI Hands-On: feram Tutorial"
  (Dec. 17/2014, Kashiwa)
- "CMSI Hands-On: modylas Tutorial"
  (Jan. 1/2015, Kobe)
- "Workshop: Programming Techniques for K-Computer"
  (Feb. 4-6/2014, Kakegawa)
- "CMSI Hands-On: SMASH Tutorial"
  (Feb. 16/2014, Kobe)
- "International Workshop on New Frontier of Numerical Methods for Many-Body Correlations --- Methodologies and Algorithms for Fermion Many-Body Problems" (Feb.18-21/2015, Hongo)
- "CMSI Hands-On: OpenMX Tutorial"
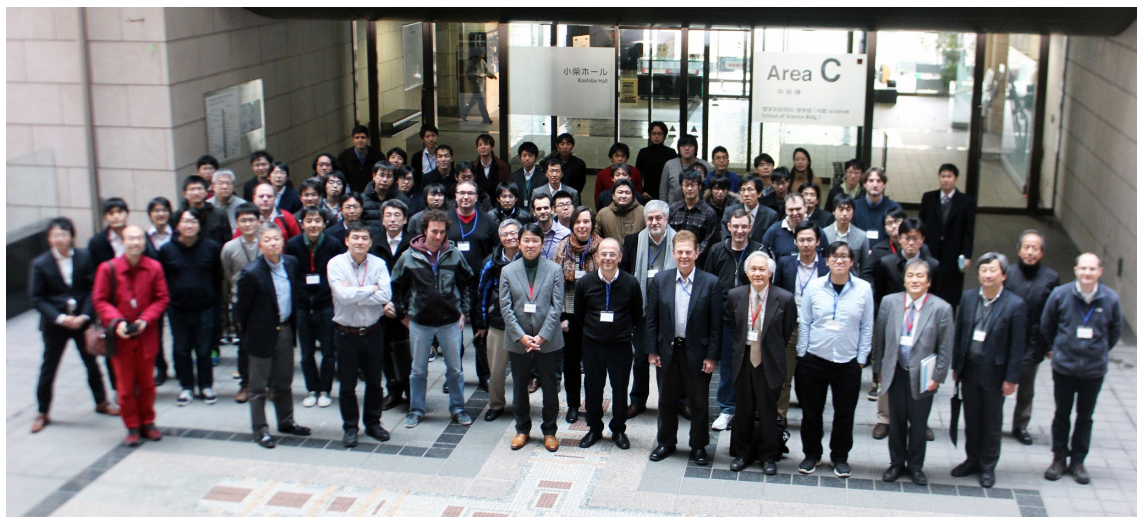 (Mar. 11/2015, Kashiwa)

Fig. 1. International Workshop on New Frontier of Numerical Methods for Many-Body Correlations, Feb.18-21/2015, Hongo

Laser and Synchrotron Research Center (LASOR Center)

Laser and Synchrotron Research (LASOR) Center started from October, 2012. LASOR Center aims to promote material sciences using advanced photon technologies at ISSP by combining the "Synchrotron Radiation Laboratory" and "Advanced Spectroscopy Group". These two groups have long histories since 1980's and have kept strong leaderships in each photon science fields for a long time in the world. In the past several decades, the synchrotron-based and laser-based photon sciences have made remarkable progresses independently. However, recent progresses in both fields make it feasible to merge the synchrotron-based and laser based technologies to develop a new direction of photon and materials sciences. In the LASOR Center, extreme laser technologies such as ultrashort-pulse generation, ultraprecise control of optical pulses in the frequency domain, and high power laser sources for the generation of coherent VUV and SX light are intensively under development. The cutting edge soft X-ray beamline is also developed at the synchrotron facility SPring-8.

LASOR center aims three major spectroscopic methods [ultrafast, ultra-high resolution, and operand spectroscopy] by three groups [extreme laser science group, soft-X-ray spectroscopy and materials science group, and coherent photon science group], as illustrated in Fig. 2. Under this framework, various advanced spectroscopy, such as ultra-
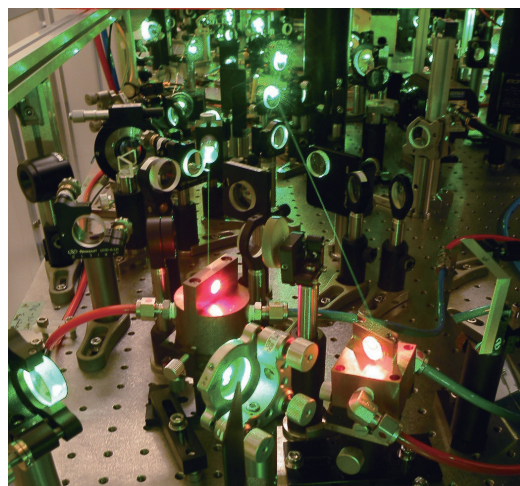

Fig. 3. Close look of a high-peak-power ultrashort-pulse laser

high resolution photoemission, time-resolved, spin-resolved spectroscopy, diffraction, light scattering, imaging, microscopy and fluorescence spectroscopy are in progress by employing new coherent light sources based on laser and synchrotron technologies that cover a wide spectral range from X-ray to terahertz. In LASOR Center, a variety of materials sciences for semiconductors, strongly-correlated materials, molecular materials, surface and interfaces, and bio-materials are studied using advanced light sources and advanced spectroscopy. Another important aim of LASOR Center is the synergy of photon and materials sciences.

Most of the research activities on the extreme laser development and their applications to materials science are performed in the ISSP buildings D and E at Kashiwa Campus where large clean rooms and the vibration-isolated floor are installed. On the other hand, the experiments utilizing the advanced synchrotron source are performed at a beamline BL07LSU in SPring-8 (Hyogo).

• Extreme Laser Science Group

The advancement of ultrashort-pulse laser technologies in the past decade has transformed the laser development at ISSP into three major directions, (i) towards ultrashort in the time domain, (ii) ultra high resolution in the spectral domain, and (iii) the extension of the spectral range, with extreme controllability of the laser sources. For ultrafast

Fig. 1. Open ceremony of LASOR center on October 2012.

Fig. 2. Developments of advanced spectroscopy at LASOR center by three groups
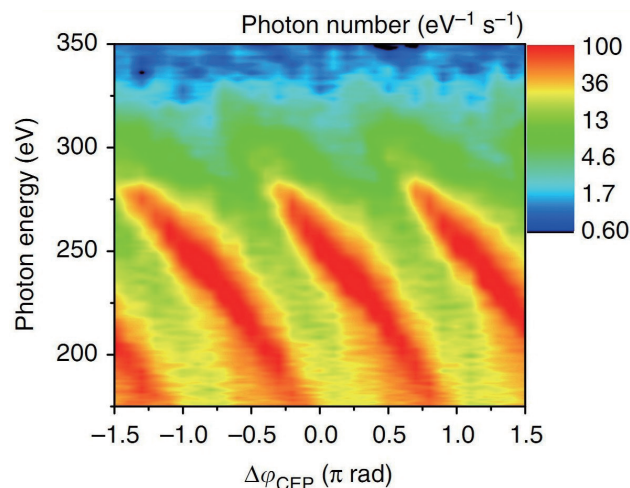

Fig. 4. Phase-dependence of high harmonic spectra in soft X rays.

Fig. 5. 10-MHz high harmonic generation in an enhancement cavity.

spectroscopy, we have developed carrier-envelope phase stable intense infrared light source that can produce sub-two cycle optical pulses for high harmonic and attosecond pulse generation. So far we observed coherent soft-X-ray radiation extending to a photon energy of ~330 eV. The simulation predicts the soft-X-ray field consists of single isolated attosecond pulses. For ultra-high resolution spectroscopy, fiber-laser-based light sources are intensively developed for producing EUV pulses for high resolution and time-resolved photoemission spectroscopy as well as extending the frequency comb to ultraviolet or infrared for various applications. The spectral range of intense optical pulses are being extended from visible to IR, MIR and THz ranges. Various types of high-repetition-rate ultrastable light sources are developed for laser-based ultrahigh resolution photoemission spectroscopy, high-average-power EUV generation in an enhancement cavity, and frequency comb spectroscopy for atomic physics, astronomical application, and frequency standards.

• Soft-X-ray and Materials Science Group

Recently, VUV and SX lasers have progressed very rapidly. They become very powerful for the materials science using the cutting-edge VUV and SX spectroscopy. Especially, angle resolved photoemission spectroscopy (ARPES) is very powerful to know the solid state properties. Laser has excellent properties, such as coherence, monochromaticity, polarization, ultra-short pulse, high intensity, and so on. By using monochromatic laser light, the resolution of ARPES becomes about 70-μeV. The materials science
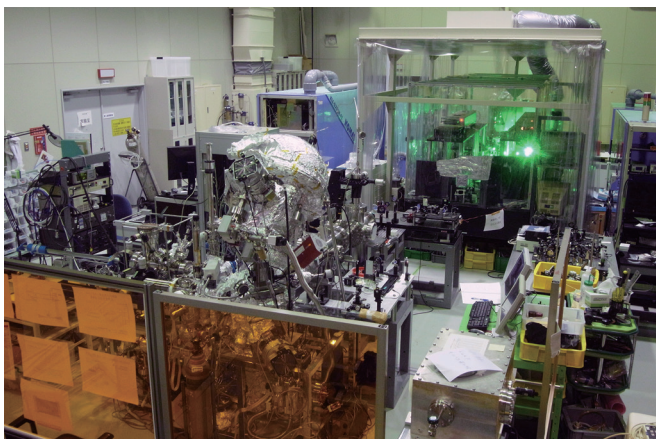

Fig. 6. Pump-probed photoemission system using 60-eV laser

with sub-meV resolution-ARPES is improved drastically by using high resolution laser. For examples, superconducting gap anisotropy of the superconductors and Fermiology of the strongly correlated materials are studied very well. On the other hand, using pulsed laser light, the time-resolved photoemission in fs region becomes powerful to know the relaxation process of photo-excited states of the materials. Furthermore, by using CW laser with circular polarization in VUV region, the photoelectron microscopy (PEEM) is developed. The spatial resolution of nm resolution is very powerful for the study of nanomagnetic materials.

• Coherent Photon Science Group

The coherent-photon science group has main interests in exploring a variety of coherent phenomena and non-equilibrium properties of excited states in condensed matters, in collaborations with research groups in charge of photoemission, operand-spectroscopy and extreme laser science. This group covers a wide range of materials, from semiconductors, ferromagnets, complexes and superconductors to biomaterials. Various ultrafast optics technologies such as femtosecond luminescence and pump-and-probe transmission/reflection spectroscopy are applied to studies on wavepacket dynamics, photo-induced phase transitions and carrier dynamics. Coherent control and observation of spin dynamics in magnetic materials and metamaterial structures by using high power terahertz radiation source is extensively studied. Advanced photonics devices are intensively studied, such as quantum nano-structure lasers with novel low-dimensional gain physics, low-power light-standard LEDs, very efficient multi-junction tandem solar cells for satellite use, and wonderful bio-/chemi-luminescent systems for wide bio-technology applications.
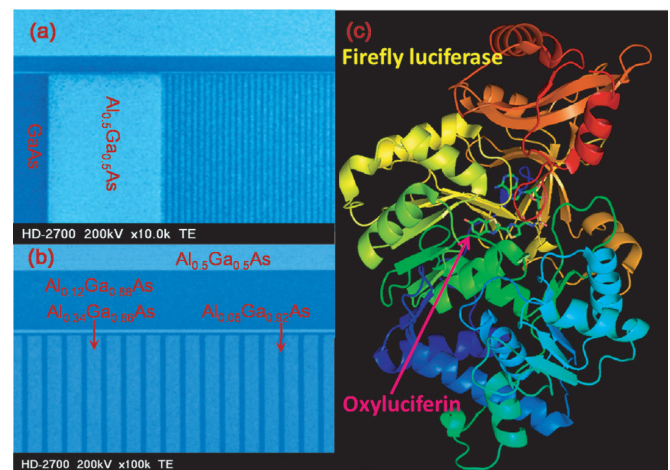

Fig. 7. Photonics devices under study: (left panel) semiconductor quantum wires and (right panel) firefly-bioluminescence system consisting of light emitter (oxyluciferin) and enzyme (luciferase)

Synchrotron Radiation Laboratory

The Synchrotron Radiation Laboratory (SRL) was established in 1975 as a research division dedicated to solid state physics using synchrotron radiation (SR). In 2006, the SRL staffs have joined the Materials Research Division of the Synchrotron Radiation Research Organization (SRRO) of the University of Tokyo and they have played an essential role in constructing a new high brilliant soft X-ray beamline, BL07LSU, in SPring-8. The light source is the polarization-controlled 25-m long soft X-ray undulator with electromagnetic phase shifters that will allow fast switching of the circularly (left, right) and linearly (vertical, horizontal) polarized photons.

The monochromator is equipped with a varied line-spacing plain grating, which covers the photon energy range from 250 eV to 2 keV. At the downstream of the beamline, a lot of experimental stations have been developed for frontier spectroscopy researches: five endstations, i.e. time-resolved soft X-ray spectroscopy (TR-SX) equipped with a two-dimensional angle-resolved time-of-flight (ARTOF) analyzer (Fig. 1), three-dimensional (3D) nano-ESCA station equipped with the Scienta R-4000 analyzer (Fig. 2), high resolution soft X-ray emission spectroscopy (XES) stations (Fig. 3) are regularly maintained by the SRL staffs and open for public use, and at free-port station many novel spectroscopic tools have been developed and installed such as soft X-ray resonant magneto-optical Kerr effect (MOKE) (Fig. 4) and soft X-ray diffraction (Fig. 5), ambient pressure photoemission, two dimensional photoelectron diffraction and so on. The beamline construction was completed in 2009 and SRL established the Harima branch laboratory in SPring-8. At SPring-8 BL07LSU, each end-station has achieved high performance: the TR-SX station have established the laser-pump and SR-probe method with the time-resolution of 50 ps which corresponds to the SR pulse-width; the 3D nano-ESCA station reaches the spatial resolution of 70 nm; the XES station provides spectra with the energy resolution around 70 meV at 400 eV and will enable real ambient pressure experiments in the near future. Soft X-ray resonant MOKE station has been developed to conduct novel
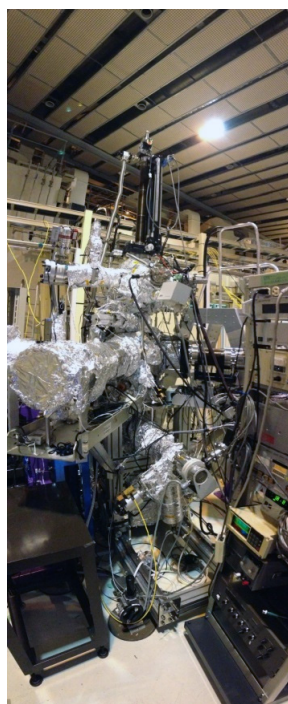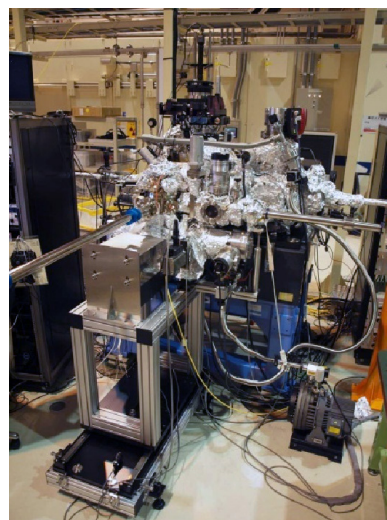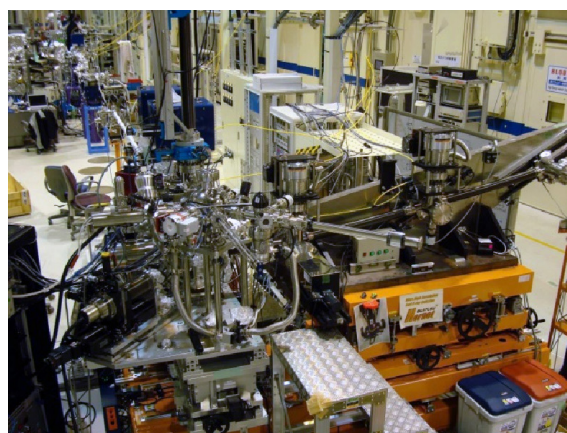

Fig. 2. 3D-nano ESCA station

Fig. 3. Soft X-ray emission station

magneto-optical experiment using the polarization-controlled 25-m long soft X-ray undulator. The soft X-ray diffraction station was connected to the beamline for the first time in February, 2015, and is preparing for time-resolved diffraction measurements. Each end-station has now been opened fully to outside users. In 2014, 150 researchers made their experiments during the SPring-8 operation time of 3400 hours.

Fig. 1. TR-SX station
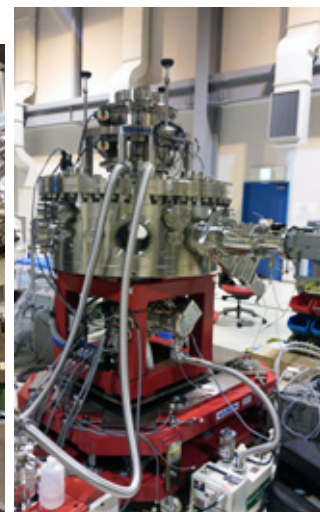

Fig. 4. Soft X-ray MOKE station

Fig. 5. Soft X-ray diffraction station

Quantum Phase near the Saturation Field in the S=1/2 Frustrated Spin Ladder

H. Yamaguchi and T. Sakakibara

Frustration in spin systems suppresses conventional magnetic orders and induces a variety of exotic quantum phenomena. Much attention has recently been paid to frustrated ferromagnets, in which ferromagnetic (FM) and antiferromagnetic (AFM) interactions strongly compete. In these systems, magnons are expected to form multiple bound states at high magnetic fields near the saturation point, owing to attractive FM interactions. Theoretical works have suggested that correlations between the bound magnons form a spin-multipolar (SM) phase and that a subsequent condensation brings about a hidden order of spin multipoles in various spin systems. Among them, the spin-nematic (quadrupolar) phase has been extensively studied as a possible candidate of the Bose-Einstein condensation of two-magnon bound states, but there is currently no clear experimental evidence of its realization. Regarding the macroscopic behavior, the magnetization curve is predicted to show an anomalous change at the phase transition to the spin-nematic order near the saturation field [1].

Here, we report on a low-temperature study of the S=1/2 organic spin ladder 3-I-V [2], which we recently succeeded in synthesizing and reported as a strong-leg spin ladder with FM leg interactions [3]. *Ab initio* molecular orbital (MO) calculations revealed that the low-temperature spin model in 3-I-V can be regarded as a weakly coupled frustrated spin ladder. Considering the magnetic and thermodynamic properties, we strongly suggest that the observed low-field phase and the phase near the saturation field are, respectively, a longitudinal spin-density-wave (SDW) order and a subsequent SM order like a spin-nematic phase.

The MO calculations indicate four kinds of additional interactions excluding those forming the spin ladder. Considering those additional interactions, we found two types of triangular units inducing frustration through the combination of the signs of the interactions. One combination consists of intraladder interactions J_{leg}, J_{rung}, and J_{diag}, and the other consists of interladder interactions J_1, J_2, and J_3, as shown in Figs. 1(a)–1(c).
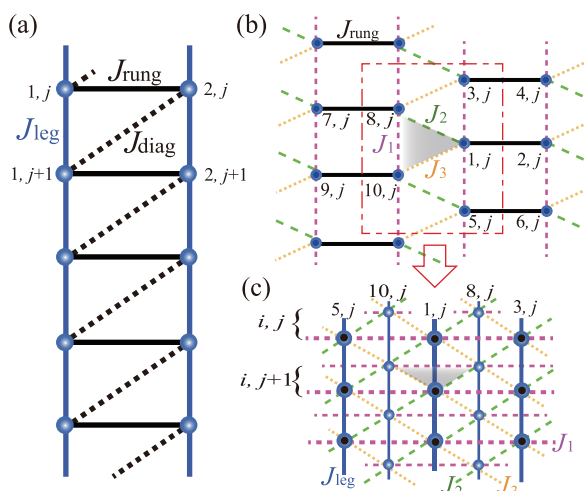
The temperature dependence of the magnetization

Fig. 1. (a) Frustrated spin ladder formed by J_{leg}, J_{rung} and the additional J_{diag} for 3-I-V. The 3D lattices connected by the interladder interactions J_1, J_2, and J_3 viewed along (b) the leg and (c) the rung directions for 3-I-V. The shadowed plane in each figure shows one of the interladder triangular units, causing frustration.
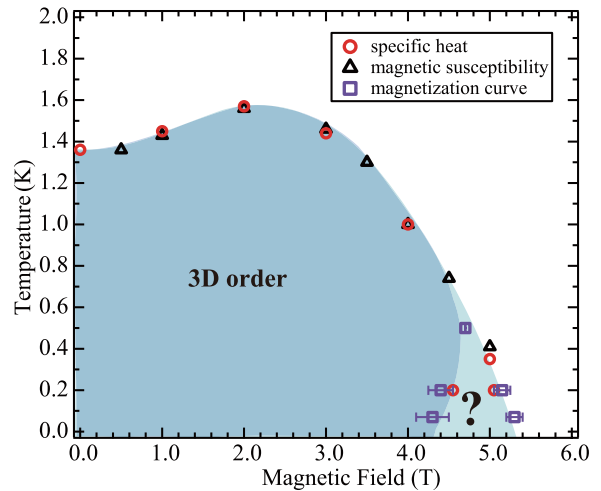

Fig. 2. Magnetic field vs temperature phase diagram showing the 3D order phase and nontrivial phase near the saturation field. The circles, triangles, and squares indicate the phase boundaries determined from the specific heat, the magnetic susceptibility, and the magnetization curve, respectively.

indicates singular cusp-like extremes [2], originating from the Bose-Einstein condensation of magnons. The specific heats consistently exhibit sharp peaks at the temperatures corresponding to these features [2]. On the other hand, we found a broad peak indicating two phase boundaries in the magnetic field dependence of the specific heat at 0.2 K. We plotted these temperatures in the magnetic field-temperature phase diagram in Fig. 2. The obtained phase diagram suggests a low-field three-dimensional (3D) order and a nontrivial phase near the saturation field. Furthermore, we found nonmonotonic behavior of the field derivative of the magnetization curve (*dM/dB*) near the saturation field [2], which suggests the existence of an intermediate phase with large quantum fluctuations just below the saturation field, as shown in Fig. 2.

We classified the low-field 3D ordered phase on the basis of the presence or absence of a successive phase transition. There is no successive phase transition in the temperature dependence of the specific heat for 3-I-V, while the corresponding curves for isomorphous 3-Cl-4-F-V and 3-Br-4-F-V indicate successive phase transitions accompanied by distinct double peaks. The absence of a successive phase transition in 3-I-V strongly suggests an SDW order with a single-component order parameter along the field direction. The presence of the SDW phase definitely indicates the formation of multi-magnon bound states [1]. Hence, the SM order is one possible explanation of the nontrivial phase near the saturation field, where the magnetization curve indicates large quantum fluctuations. For 3-I-V, the enhanced frustration effect originating from the FM diagonal interaction is considered to stabilize multi-magnon bound states.

References
[1] T. Hikihara, L. Kecke, T. Momoi, and A. Furusaki, Phys. Rev. B **78**, 144404 (2008)
[2] H. Yamaguchi, H. Miyagai, Y. Kono, S. Kittaka, T. Sakakibara, K. Iwase, T. Ono, T. Shimokawa, and Y. Hosokoshi, Phys. Rev. B **91**, 125104 (2015).
[3] H. Yamaguchi, H. Miyagai, T. Shimokawa, K. Iwase, T. Ono, Y. Kono, N. Kase, K. Araki, S. Kittaka, T. Sakakibara, T. Kawakami, K. Okunishi, and Y. Hosokoshi, J. Phys. Soc. Jpn. **83**, 033707 (2014).

Authors
H. Yamaguchi[a], H. Miyagai[a], Y. Kono, S. Kittaka, T. Sakakibara, K. Iwase[a], T. Ono[a], T. Shimokawa[b], and Y. Hosokoshi[a]
[a]Osaka Prefecture University
[b]Osaka University

Magnetic Ordering in the Ising Frustrated Spin-Chain Magnet NaCo(acac)₃benzene

Y. Karaki, S. Nakatsuji, and Y. Uwatoko

Geometrical frustration in antiferromagnets has attracted much attention in recent years. The geometrical frustration destroys the conventional Néel state and tends to produce an exotic magnetic phase. Ising spin system with antiferromagnetic nearest-neighbor interactions on a triangular lattice is a simple frustrated system. A partially disordered antiferromagnetic (PDA) phase is a typical example of such exotic phases. [1]

A series of metal chelate compounds having the formula $M^I M^{II}$(acac)₃benzene, where acac represents acetylacetonate, M^I is Na^+ or K^+ and M^{II} is divalent metal ion surrounded by the octahedron of oxygen atoms, have a trigonal crystal structure belonging to the space group *P-31c* with a = 10.24 Å and c = 11.95 Å [2]. Since the divalent metal ions form a hexagonal lattice, these compounds are possible candidates for studying the frustration on the triangular lattice.

Here we report on the results of the susceptibility(χ), magnetization and specific heat measurements using single crystals of NaCo(acac)₃benzene [2]. ESR and χ measurements (*T*>2 K) show that Co^{2+} of NaCo(acac)₃ benzene has the anisotropic *g*-factor g_c= 8.12 and g_{perp}= 1.41 for fictitious spin *S*=1/2. Figure 1(a) shows the temperature dependence of DC χ parallel to the c-axis at *H*= 5.0 Oe. The inset shows the inverse of AC $\chi(T)$ of a needle-shaped sample. Figure 1(b) shows the specific heat at zero field and DC χ at low temperatures. A long range ordering accompanied with a sudden increase of χ appears around 62 mK. Figure 2(a) shows the magnetization curve. Below 60 mK an anomaly of the *M-H* curve appears. A step-wise change of the magnetization becomes clear at 20 mK. At *H*~ 300 Oe the magnetic moment aligns fully with applied field. The plateau at 1/3 of full moment suggests a ferrimagnetic alignment of the ferromagnetic chains. The ferromagnetic intra-chain interaction J_C/k_B= -0.2 K and the antiferromagnetic inter-chain interaction J/k_B = 0.05 K are deduced from the Weiss temperature 20 mK and the critical field 300 Oe. These results confirm the 1-D nature of NaCo(acac)₃benzene. When a 1-D short-range order is well developed at low temperatures, each chain behaves like a magnetic moment and thus a magnetic ordering with two-dimensional character is expected. The mean field theory of a triangular Ising lattice predicts a step-like increase of χ at Tc from a paramagnetic phase to a PDA phase and no anomaly at Tc from the paramagnetic phase to the ferrimagnetic phase [2]. Thus the observed χ anomaly
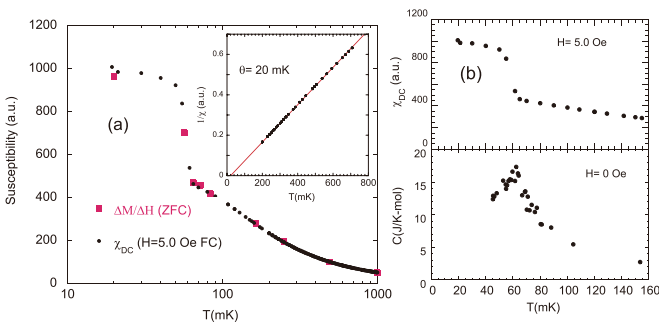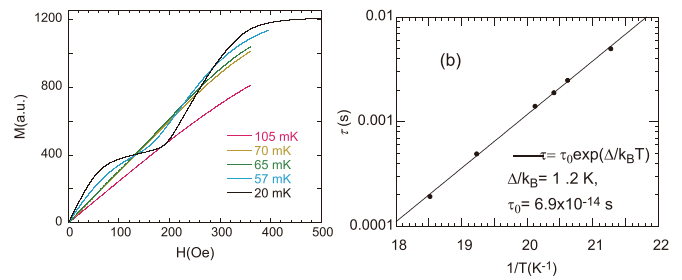

Fig. 2. (a) Magnetization curve for *H// c* at 20mK, 57mK, 65 mK and 105 mK. (b) Temperature dependence of the spin relaxation time.

at 62 mK suggests the existence of the PDA phase around zero field. At the PDA phase, two thirds of chains order into an antiferromagnetic alignment and the resultant chain is incoherent with other chains. Since the molecular fields of the incoherent chain are canceled, the magnetic response of single chain is expected in the PDA phase. Figure 2(b) shows temperature dependence of the spin relaxation time obtained from the frequency dependence of AC χ. The thermal activation process with the gap energy Δ/k_B= 1.2 K is observed. However, obtained gap energy is about 6 times larger than estimated value using $\Delta=4S^2 Jc$ given by Glauber for a ferromagnetic Ising chain [3]. The simple chain model in the PDA phase cannot explain the observed spin relaxation well enough. Further microscopic measurements are necessary to clarify the ordered phase and the spin relaxation mechanism.

References
[1] M. Mekata, J. Phys. Soc. Jpn. **42**, 76 (1977).
[2] Y. Karaki, K. Kuga, K. Kimura, S. Nakatsuji , K. Matsubayashi, and Y. Uwatoko, submitted to J. Phys. Soc. Jpn.
[3] R. J. Glauber, J. Math. Phys. **4**, 294 (1963)

Authors
Y. Karaki[a], K. Kuga[b], K. Kimura[b], S. Nakatsuji , K. Matsubayashi, and Y. Uwatoko
[a]University of the Ryukyus
[b]Osaka University

Fig. 1. (a) Temperature dependence of DC χ (FC) and differential χ obtained from *M-H* curves. *M-H* curves are measured after zero field cooling. The inset shows the inverse of AC χ (220 Hz) of a needle-shaped sample at *T*> 200 mK. (b) Temperature dependence of the specific heat at zero field and DC χ at 5.0 Oe below 160 mK.

Trivial Yet Distinct

Y. Fuji, F. Pollmann, and M. Oshikawa

Classification of quantum phases is a central subject in statistical mechanics and condensed matter physics. Traditionally, it was based on the notion of spontaneous symmetry breaking, as initiated by Landau. However, recently, a rich variety of quantum phases without any spontaneous symmetry breaking has been recognized. This also requires us to develop new concepts and formulations. One of the novel classes of quantum phases is called Symmetry-Protected Topological (SPT) phases. As the name suggests, they are distinct from the trivial phase only in the presence of an appropriate symmetry. In this regard, SPT phases are similar to the conventional ordered phases with a spontaneously broken symmetry. However, SPT phases do not break the symmetry, and hence are called topological. A well-known example of SPT phases is the topological insulator, which possesses a helical edge state and is distinct from a trivial band insulator. The helical edge state and the distinction from a trivial band insulator however go away once the time-reversal symmetry is broken explicitly. Another example of SPT phases is Haldane phase in *S* =1
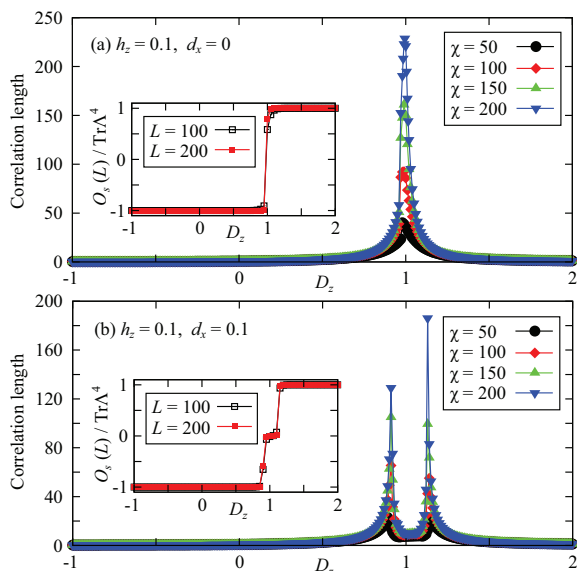
Fig. 1. Divergence of the correlation length demonstrating the existence of the quantum phase transition separating the two trivial phases. Insets show the non-local string order parameter which distinguishes the two phases.

antiferromagnetic chains. There is no long-range order which can be detected by a local order parameter in the Haldane phase. Nevertheless, the Haldane phase is separated by a quantum phase transition from a trivial phase such as "large-D phase" which includes the product of $S^z = 0$ states. The Haldane phase also has a characteristics of edge state (free spin), which is protected by the time-reversal symmetry. It turns out however that the edge states are not the most general characterization of SPT phases. Under the lattice inversion symmetry, there are topological insulator and Haldane phase without any physical edge state. These are most generally characterized by degeneracy in the entanglement spectrum. This implies that they are distinct, in the presence of the symmetry, from a trivial product state without any entanglement.

In a recent joint research [1] we demonstrated that the notion of symmetry protection of quantum phases can be generalized in a somewhat surprising manner. In the standard SPT phases, as we discussed above, there is a nontrivial entanglement which makes the state distinct from a trivial product state. We showed that, in the presence of a certain class of inversion symmetry, there are two trivial phases that are still distinct, in a simple model of $S = 1$ chain. By "trivial phase" we mean the ground state can be adiabatically connected to a product state where there is no entanglement at all. Nevertheless the two trivial phases are distinct in the sense that they are always separated by a quantum phase transition as long as the symmetry is kept. We dubbed them "Symmetry-Protected Trivial (SPt)" phases. We have also formulated a non-local string order parameter which can distinguish these phases and detect the quantum phase transition between them. So, there is something nontrivial even in trivial phases! This would also add a new aspect to the fundamental question "What is phase?".

This work was performed in collaboration between ISSP and Max-Planck Institute for Physics of Complex Systems, which is recently strengthened by the JSPS Strategic International Networks Program No. R2604 "TopoNet."

Reference
[1] Y. Fuji, F. Pollmann, and M. Oshikawa, Phys. Rev. Lett. **114**, 177204 (2015).

Authors
Y. Fuji, F. Pollmann[a], and M. Oshikawa
[a]Max-Planck Institute for Physics of Complex Systems

First-Principles Simulation Program for Excited States

Y. Noguchi, M. Hiyama, and N. Koga

These days the first-principles simulations are commonly used as a basic tool for the material research. Most of the simulation programs have been designed for the ground state only, while excited states are the target of increasing number of spectroscopic measurements demanding thereby the program to cover the excited states. Recently, Noguchi, Hiyama and Koga have shown such extension is possible with the first-principles two-particle Green's function program.

The program has been developed by Noguchi on the basis of the Bethe-Salpeter equation (BSE) combined with the GW approximation (GWA) to the self-energy operator, and the problem originated from the extremely large computational requirement has been overcome by the development of the parallel programming. Thus the remaining problem is to test the accuracy of the program by comparing with reference data and convince it to the users of the first-principles program. In this context, the authors focused on recently synthesized nanomaterials, or the fullerene containing alkali metal inside and a carbon material called warped nanographene, which are extraordinarily suitable for the benchmark. By comparing the measured and calculated spectra, reliability of the GW-BSE calculation was shown [1, 2].

More stringent test was done for the core-excitation spectrum of a molecule [3], which so far has been calculated using the density functional theory together with empirical
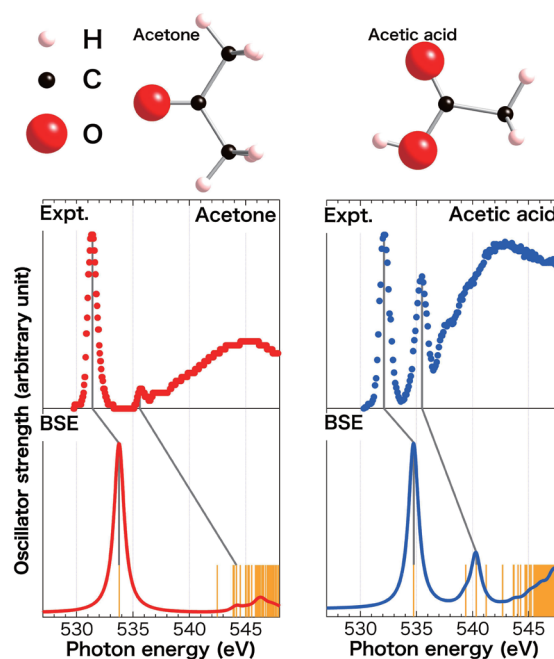

Fig. 1. Comparison of the calculated (bottom) and the measured (top) XAS spectra for benchmark molecules, acetone (left) and acetic acid (right). Using the first-principles Green's function scheme, the excitation energy from the oxygen 1s state to the valence states was calculated for the first time without empirical parameters. The calculated excitation energies are in agreement with experiments within the error of 1 %, or 2-5 eV. This demonstrates that theory is able to provide reliable data that will help analyzing the measurements.

adjustments. By the comparative study, the authors demonstrated that x-ray absorption spectra (XAS) can be reliably assigned fully from first-principles using the program (see Fig. 1).

So far, the program was also applied to other materials such as the firefly liciferin, or the light-emitting compound found in firefly species, to understand the light-emitting mechanism [3]. The GW-BSE program is planned to open to ISSP supercomputer users and is expected to advance our understanding of the excited states of materials.

References
[1] Y. Noguchi, O. Sugino, H. Okada, and Y. Matsuo, J. Phys. Chem. C **117**, 15362 (2013).
[2] Y. Noguchi and O. Sugino, J. Chem. Phys. **142**, 064313 (2015).
[3] Y. Noguchi, M. Hiyama, H. Akiyama, N. Koga, J. Chem. Phys. **141**, 044309 (2014).
[4] Y. Noguchi, M. Hiyama, H. Akiyama, Y. Harada, and N. Koga, J. Chem. Theor. Compt. **11**, 1668 (2015).

Authors
Y. Noguchi, M. Hiyama, and N. Koga[a]
[a]Nagoya Univerisy

Dephasing in Single-Electron Generation Due to Environmental Noise Probed by Hong-Ou-Mandel Interferometry

E. Iyoda, T. Kato, K. Koshino, and T. Martin

Quantum mesoscopic physics, or nanophysics, aims at studying the manifestations of quantum mechanics, such as interference effects and coherence, with electron transport in condensed matter materials. Such manifestations have been studied in the context of quantum optics since the middle of the past century, where fundamental tests of quantum mechanics were explored, for instance, in Hanbury Brown and Twiss [1] (HBT) and Hong-Ou-Mandel [2] (HOM) experiments for photons. The fermionic counterpart of the HOM experiment has been realized quite recently in a setup of a two-electron collider using a quantum point contact (QPC) and two single-electron generators composed of integer quantum Hall edge states and quantum dots [3] (see a schematic figure in Fig. 1(a)). In the fermionic HOM experiment, if two electrons arrive at the QPC simultaneously, the two electrons always scatter into two different output channels because of their fermionic statistics.

In condensed matter settings, the two electrons are always accompanied by the Fermi sea, and as charged particles they interact strongly between themselves and with their environment. The coherence of injected electrons is directly measured by perfectness of anti-correlated scattering in the fermionic HOM experiment. The imperfect anti-correlated scattering reported in [3] includes information about the distinguishability of propagating electrons in the chiral edge channels before arriving at the QPC. At present, the dephasing of propagating electrons has been discussed mostly by considering Coulomb interactions between electrons. The origin of electron decoherence has, however, not yet been determined experimentally. We have examined the effect of electron decoherence by focusing on the role of the energy-level fluctuations of the quantum dot due to this environment [4].

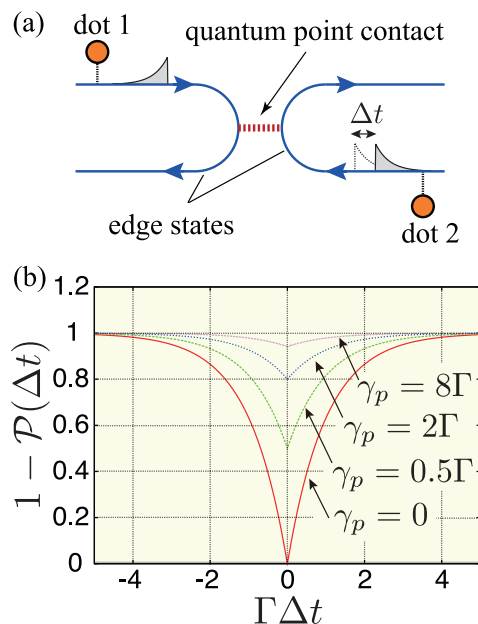We have employed a simple analytic framework for

Fig. 1 (a) A schematic figure of the Hong-Ou-Mandel-type two-electron collision experiment. Two electrons injected from two quantum dots propagate along edge states of integer quantum Hall states, and collides at a central quantum point contact (QPC). (b) The probability $1-P(\Delta t)$, that two electrons scatter into the same edge states, is plotted as a function of a wavepacket delay time Δt. Two electrons always scatter into difference edge states ($1-P(\Delta t) = 0$) when $\Delta t = 0$ and $\gamma_p = 0$. On the other hand, as the dephasing rate γ_p increases, the probability $1-P(\Delta t)$ at $\Delta t = 0$ increases, and approaches the classical value.

evaluating the current noises reflecting electron indistinguishability based on the so-called input-output relation, which is a standard theoretical tool in quantum optics. In this approach, the dephasing rate γ_p due to energy-level fluctuations is easily taken into account in the model Hamiltonian. In order to clarify coherence of generated electrons, we have calculated $P(\Delta t) = \mathrm{Tr}(\rho(t)\rho(t+\Delta t))$, where $\rho(t)$ is a density matrix of injected electrons and Δt is the time delay between the two emitted electron wave packets (see Fig. 1(a)), and have obtained an analytic solution, $P(\Delta t) = 1/(1+ \gamma_p/\Gamma) \exp(-\Gamma|\Delta t|)$ where Γ is the decay time of electron generators. Figure 1(b) shows a plot of $1-P(\Delta t)$, which is proportional to the excess current noise measured at one of the output channels, assuming a balanced transmissivity of QPC. If there is no dephasing ($\gamma_p = 0$), the excess noise is completely suppressed for the simultaneous collision ($\Delta t = 0$) between injected electrons. This is the manifestation of the Fermi statistics of the injected electrons. As the pure dephasing rate γ_p increases, the dip of the current noise is reduced and vanishes for $\gamma_p \gg \Gamma$. We note that $\mathcal{P} = P(0)$ corresponds to the purity $\mathcal{P} = \mathrm{Tr}(\rho^2)$ of injected electrons, which has the simple form in our case: $\mathcal{P} = \Gamma/(\Gamma+ \gamma_p)$. The purity approaches 1 for $\gamma_p \ll \Gamma$, leading to a perfect suppression of the excess noise.

In our work [4], we have also shown that the time filtering technique helps to enhance the purity, and that a generalization of the present results to an asymmetric setup is possible, with possible implication for measuring the energy detuning of the two injectors in actual experiments. Our calculation provides a useful and comprehensive picture of dephasing effects on the quality of generated single electrons as well as compact formulas for the purity and the current noises in the HOM experiment.

References
[1] R. H. Brown and R. Q. Twiss, Proc. R. Soc. A **242**, 300 (1957).
[2] C. K. Hong, Z. Y. Ou, and L. Mandel, Phys. Rev. Lett. **59**, 2044 (1987).
[3] E. Bocquillon *et al.*, Science **339**, 1054 (2013).
[4] E. Iyoda, T. Kato, K. Koshino, and T. Martin, Phys. Rev. B **89**, 205318 (2014).

Authors
E. Iyoda[a], T. Kato, K. Koshino[b], and T. Martin[c]
[a]University of Tokyo
[b]Tokyo Medical and Dental University
[c]Aix Marseille Université, CNRS, CPT

Fig. 2. Low field magnetoconductance with current along the steps exhibits oscillatory behavior superposed on the positive magnetoconduction attributable to the weak localization effect. The vertical dashed lines marked by arrows represent the expected positions of open orbit geometrical resonance.

Electrical Conduction in Epitaxial Graphene on Stepped Substrate of Vicinal SiC Surface

A. Endo, F. Komori, and S. Tanaka

Two-dimensional electron system (2DES) in graphene, *i.e.* a single or a few layers of graphitic sheet, has attracted much interest on account of its properties quite distinct from conventional 2DES. Graphene samples are typically produced either by "peel-and-stamp" technique or by epitaxial growth on appropriate substrates. In this study[1] monolayer graphene was grown on a vicinal surface of 6H-SiC(0001) which has a quasi-regular step-and-terrace structure as shown in Fig.1. This is analogous to 2DES in a GaAs/AlAs quantum well fabricated on the (775)B surface of GaAs [2].

Electrical conduction under a magnetic field normal to the plane showed a high degree of anisotropy. The quantum Hall effect (QHE) with zero resistance manifests itself for the current along the steps as shown in Fig.1, whereas the QHE is obscured by pronounced positive magnetoresistance with quadratic magnetic-field dependence for the current across the steps. The latter, as well as the small slope of the Hall resistance, implies the presence of parallel conduction due to remnant carriers in the SiC substrate, albeit with seeming inconsistency with the zero resistance observed for the former current direction. The anisotropic behavior is interpreted by assuming that the parallel conduction is sizable along the steps but is virtually prohibited across the steps

Conspicuous negative magnetoresistance in low field regime can be analysed by the weak localization formula. The phase relaxation time τ_ϕ thus obtained is on the order of a few psec, which considerably exceeds the transport relaxation time $\tau \sim 10^{-2}$ psec. The conductance along the steps is found to exhibit small-amplitude oscillations as shown in Fig. 2, after subtracting out the large positive magnetoconductance of the weak localization origin. This oscillatory behavior is attributed to open-orbit geometrical resonance effect previously elucidated in a GaAs/AlGaAs 2DES subjected to a unidirectional potential modulation [3].

References
[1] A. Endo, F. Komori, K. Morita, T. Kajiwara, and S. Tanaka, J. Low Temp. Phys. **179**, 237 (2015).
[2] Y. Iye, A. Endo, S. Katsumoto, Y. Ohno, S. Shimomura, and S. Hiyamizu, Physica E **12**, 200 (2002).
[3] A. Endo and Y. Iye, Phys. Rev. B **71** 081303(R) (2005).

Authors
A. Endo, F. Komori, K. Morita[a], T. Kajiwara[a], and S. Tanaka[a]
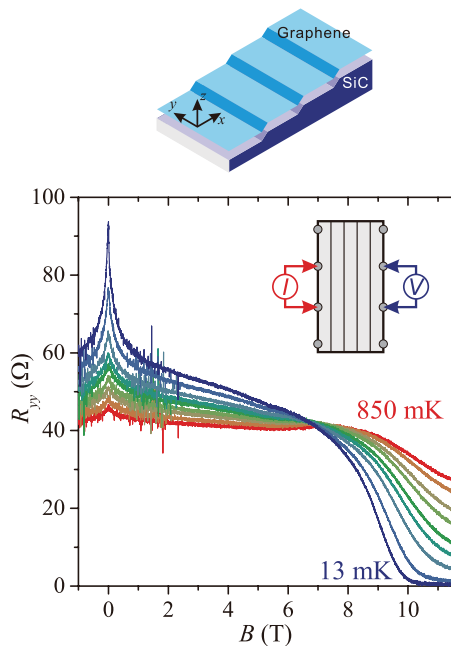[a]Kyushu University

Fig. 1. Epitaxial monolayer graphene grown on a vicinal surface of 6H-SiC(0001) which has a regular step-and-terrace structure. Resistance along the step exhibits negative magnetoresistance characteristic of weak localization at low field and well-developed quantum Hall effect (ν=2) at high field.
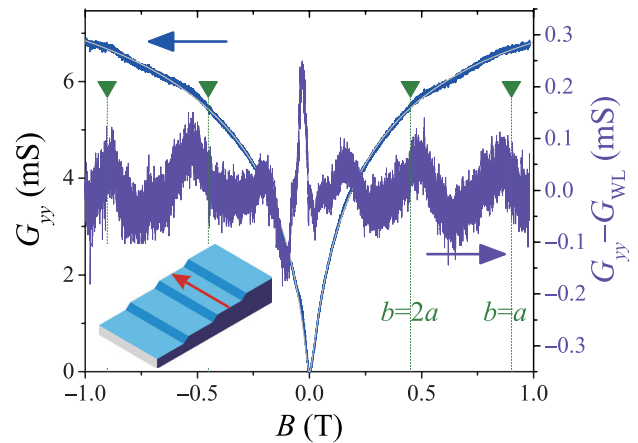
Methylation of Epitaxial Graphene on SiC(0001) through Two-Step Chlorination Alkylation Reactions

Md. Z. Hossain and J. Yoshinobu

Chemical modification of graphene with varieties of functionalities is vital for anticipated applications such as sensing, detecting, and composite material systems. However, it is not easy to chemically graft the atoms or molecules onto the graphene surface because of the bonding nature of sp^2 C atoms in graphene. Therefore, it is highly desirable to establish a common chemical approach through which the pristine graphene can be modified with varieties of chemical species. In this joint research, we demonstrate the covalent binding of a methyl group on the basal plane

of epitaxial graphene on SiC(0001) through the two-step chlorination and alkylation processes using a Grignard reagent (CH_3MgBr). The modified surfaces are characterized by scanning tunneling microscopy and spectroscopy, X-ray photoelectron spectroscopy (XPS) and Raman spectroscopy.

Figure 1a is an atomic resolution STM image of monolayer epitaxial graphene (EG) on SiC(0001). The hexagonal network of the graphene lattice is clearly seen over the $6\sqrt{3} \times 6\sqrt{3}$ substrate structure. The chlorination of EG was done by exposing the surface to Cl_2 under UV light in N_2 atmosphere. Following the chlorination of graphene, the atomically resolved high-resolution image clearly reveals that the EG contains a large number of small protrusions (Figure 1b). Since the graphene mesh and underlying substrate periodicity are still visible, we ascribe these additional small protrusions to the chemisorbed Cl atoms on EG. Note that the surface morphology shown in Figure 1b is only seen in the monolayer EG region. Figure 1c shows a typical STM image; the hexagonal mesh of the graphene lattice is clearly visible in the lower half of the image, and the upper half contains randomly distributed protrusions ascribed to the chemisorbed Cl. The approximate surface coverage of chemisorbed Cl is estimated to be ~ 8 atom%. Based on the atomic resolution STM and Raman measurements on the different areas of the surface, we conclude that chemisorption of Cl is selective to the monolayer EG on SiC.

The covalent binding of Cl onto the EG is confirmed by the XPS spectra as shown in Figure 1d. The Cl 2p and Cl 2s peaks are observed in the XPS spectrum for chlorinated graphene (Fig. 1d(ii)). The high-resolution Cl 2p spectrum exhibits two components at 200.2 and 201.8 eV (Fig. 1e). When the chlorinated EG is treated with CH_3MgBr in THF, the Cl peaks disappear [Figure 1d(iii), e(iii)] and the height of the C 1s peak slightly increased [Figure 1d(iii)] compared to that of the chlorinated surface. The absence of any Mg or Br peaks in the wide range spectra suggests the clean EG modified with only the C containing group. The STM investigations of CH_3MgBr treated surfaces indicate that only the monolayer graphene regions contain small protrusions randomly distributed over the surface. The density of small protrusions is similar to that of the respective chlorinated
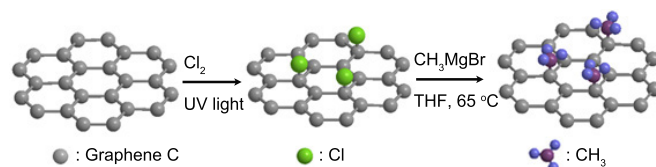

Fig. 2. Schematic of the reaction steps for photochlorination and methylation of epitaxial graphene on SiC using CH_3MgBr in THF. [© 2014 American Chemical Society]

surface. A typical atomically resolved STM image of the CH_3MgBr treated surface is shown in Figure 1f. In addition to the small protrusions, we can clearly see the underlying hexagonal mesh of graphene in Fig. 1f. These small protrusions are found to be stable even after annealing the surface at 300 °C in UHV. Since the surface is free from any other contamination as revealed by XPS, we ascribed these small protrusions to the covalently bonded CH_3 groups.

The scheme for the present two-step reactions is summarized in Fig. 2, and the detailed analysis of experimental data and discussion is found in reference 1.

Reference
[1] Md. Z. Hossain, M. B. A. Razak, H. Noritake, Y. Shiozawa, S. Yoshimoto, K. Mukai, T. Koitaya, J. Yoshinobu, and S. Hosaka, J. Phys. Chem. C **118**, 22096 (2014).

Authors
Md. Z. Hossain, M. B. A. Razak, H. Noritake, Y. Shiozawa, S. Yoshimoto, K. Mukai, T. Koitaya, J. Yoshinobu, and S. Hosaka

Imaging of Josephson Vortices on Surface Superconductor by Scanning Tunneling Microscopy

T. Uchihashi, X. Hu, and Y. Hasegawa

The recent discovery of superconductivity in silicon surface reconstructions with metal adsorbates was an unexpected surprise, and as an ultimately thin 2D superconductor extensive studies on their properties are in progress [1-4]. One ubiquitous feature of these systems is the presence of atomic steps, which may strongly affect electron transport there. Recent direct electron transport measurements indicated that atomic steps work as Josephson junctions [2]. Nevertheless, direct evidence of Josephson coupling has not been obtained yet, and possible local variation of its strength has remained an open issue.

Here, we report on compelling evidence of the Josephson coupling at atomic steps on the surface superconductor Si(111)-($\sqrt{7} \times \sqrt{3}$)-In [5]. Zero-bias conductance (ZBC) images, which correspond to a mapping of the density of states (DOS) at the Fermi level, taken with a low-temperature scanning tunneling microscopy (STM) reveal that vortices are present at atomic steps after magnetic fields are applied. Elongated shapes and significant recovery of superconductivity within their cores, which are characteristic to Josephson vortices (JV), are clearly observed in the images.

Figure 1(a) shows an STM image with an area of 500 nm×1500 nm. The surface consists of flat terraces separated by single atomic height steps. ZBC images taken on the same area under magnetic fields of 0.08, 0.04, 0 T are displayed in Figs. 1(b)-1(d). The imagings were performed
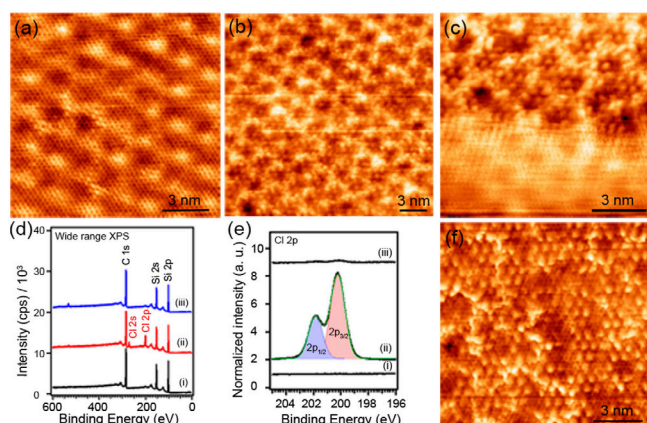

Fig. 1. Typical ambient STM images of (a) the clean epitaxial graphene on the Si-face of the SiC substrate and (b) the same surface after chlorination. (c) Chlorinated and non-chlorinated areas within the same scanning area. (d) Wide range XPS spectra of (i) clean, (ii) chlorinated, and (iii) chlorinated surface treated with CH_3MgBr in THF (tetrahydrofuran) for 2 h at 65 °C. hν = 1486 eV. (e) High-resolution Cl 2p XPS spectra of (i) clean, (ii) chlorinated, and (iii) chlorinated surface treated with CH_3MgBr in THF. hν = 410 eV. (f) Atomic resolution STM image of the chlorinated surface treated with CH_3MgBr. V_{tip} = 0.5 V; I_{tunnel} = 0.5 nA. [© 2014 American Chemical Society]
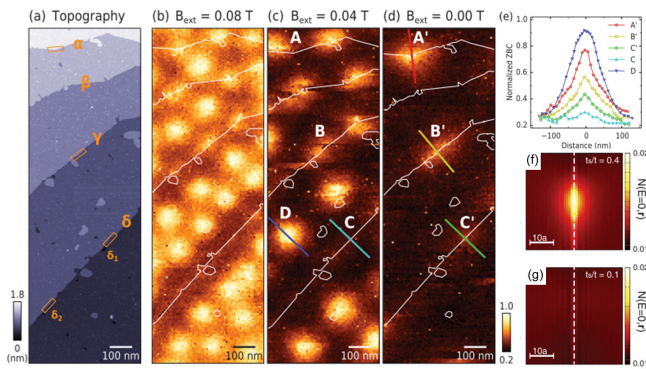
Fig. 1. (a) Large-scale STM image of Si(111)-($\sqrt{7} \times \sqrt{3}$)-In surface, where the terraces are separated by atomic steps marked as α, β, γ, and δ from top to bottom. (b)-(d) ZBC images taken under magnetic fields of (b) 0.08 T, (c) 0.04 T, (d) 0 T. The positions of the atomic steps are depicted by thin solid lines. (e) Spatial profiles of ZBC plotted along the thick solid lines shown in (c) and (d). (f) and (g) numerically obtained spatial profile of the zero energy DOS for the hopping strength $t_s/t = 0.4$ and 0.1, respectively. The dashed lines indicate the place where the Josephson coupling was modeled.

below 0.5 K, which is sufficiently lower than $T_c \approx 3$ K of the superconducting surface. At 0.08 T, round vortices formed a closely packed triangular lattice within each terrace. Reduction of the magnetic field to 0.04 T decreased the number of vortices as expected. When the magnetic field was set to zero, vortices disappeared from the terraces, but slightly bright regions remained along the steps [Fig. 1(d)]. Note that similar features were also present along the steps at finite fields [Figs. 1(b) and 1(c)]. They are not simply regions where superconductivity is suppressed due to the presence of steps because the features change their positions under different magnetic fields, as seen from A and A'. These observations clearly show that these bright features are vortices trapped at the atomic steps.

The vortices at steps are anomalous compared to the vortices on terraces. First, their shapes are elongated along the steps whereas the vortices on terraces are round. Second, ZBC values measured at the centers are lower than those of the vortices on terraces, as quantitatively depicted in Fig. 1(e). These anomalies are the direct consequences of JV and show that the atomic steps work as Josephson junctions.

Suppose that a vortex is created by penetration of the magnetic field through a Josephson junction line and its surrounding region. At the junction, the critical current density J_c is suppressed from that of the superconducting regions J_0. This leads to two important properties regarding the vortex [6]. First, the circulation of supercurrent near the center is strongly deformed and the vortex core is elongated along the junction line by a factor of $(J_c/J_0)^{-1}$. Second, the breaking of superconductivity around the core is weakened as J_c/J_0 decreases. When the supercurrent distribution near the junction line is nearly parallel and the suppression is sufficiently small, the vortex should be called a JV, like the case of layered superconductors under magnetic field parallel to the layers [7].

To ensure this picture, we numerically calculated the order parameter and DOS using the Bogoliubov-de Gennes (BdG) equation for a 2D tight-binding model with the hopping strength t_s at the Josephson junction reduced from a constant hopping strength t elsewhere. Then the Josephson parameter J_c/J_0 is represented by the ratio t_s/t. Figures 1(f) and 1(g) display zero-energy DOS calculated for $t_s/t = 0.4$ and 0.1, respectively. The characteristics of zero-energy DOS are different from the case of

$t_s/t = 1$; its magnitude around the center is decreased as t_s/t is reduced, while the spatial distribution becomes strongly elliptic, which directly corresponds to the observed changes for vortices A', B', and C' in Fig. 1(d). From the comparison of the experiment and the theory, J_c/J_0 is estimated to be ~ 0.4 for step γ where vortex B' is located. Because of a weaker coupling at step δ, vortex C' can be safely called a JV.

References
[1] T. Zhang *et al.*, Nat. Phys. **6**, 104 (2010).
[2] T. Uchihashi, P. Mishra, M. Aono, and T. Nakayama, Phys. Rev. Lett. **107**, 207001 (2011).
[3] M. Yamada, T. Hirahara, and S. Hasegawa, Phys. Rev. Lett. **110**, 237001 (2013).
[4] C. Brun *et al.*, Nat. Phys. **10**, 444 (2014).
[5] S. Yoshizawa, H. Kim, T. Kawakami, Y. Nagai, T. Nakayama, X. Hu, Y. Hasegawa, and T. Uchihashi, Phys. Rev. Lett. **113**, 247004 (2014).
[6] G. Blatter, M. V. Feigel'man, V. B. Geshkenbein, A. I. Larkin, and V. M. Vinokur, Rev. Mod. Phys. **66**, 1125 (1994).
[7] P. J. W. Moll, L. Balicas, V. Geshkenbein, G. Blatter, J. Karpinski, N. D. Zhigadlo, and B. Batlogg, Nat. Mater. **12**, 134 (2013).

Authors
S. Yoshizawa[a], H. Kim, T. Kawakami[a], Y. Nagai[b], T. Nakayama[a], X. Hu[a], Y. Hasegawa, and T. Uchihashi[a]
[a]International Center for Materials Nanoarchitectonics, National Institute for Materials Science
[b]CCSE, Japan Atomic Energy Agency

Silver Oxide Clathrate Thin Films

Y. Matsumoto, R. Takahashi, and M. Lippmaa

We have studied the possibility of growing epitaxial films of silver clathrates on single-crystal oxide substrates by photoelectrochemical deposition. The clathrates chosen for this study were $Ag_7O_8NO_3$ and $Ag_7O_8HSO_4$. Both materials consist of a cubic lattice of Ag_6O_8 cages that enclose either NO_3 or HSO_4 anions, as illustrated in Fig. 1(a). Silver clathrates have various interesting properties; $Ag_7O_8NO_3$, for example, becomes superconducting at 1 K. Our purpose was to develop a technique for fabricating epitaxial clathrates with well-defined orientation on a single-crystal substrate. Silver clathrates contain Ag ions in several valence states, including Ag^+, Ag^{2+}, and Ag^{3+}, which means that strongly oxidizing synthesis conditions are needed. One possibility is to use photoelectrochemical deposition on a metallic substrate under a suitable substrate bias in either $AgNO_3$ or Ag_2SO_4 solution. Growth experiments on 0.5 wt% Nb-doped TiO_2 substrates showed that the best selectivity for clathrate
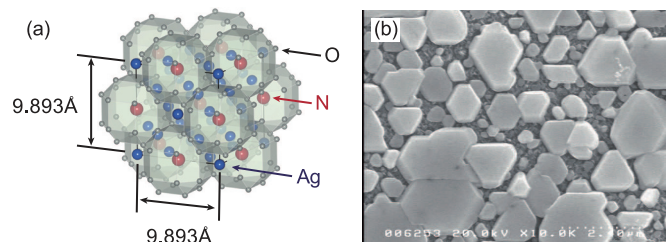

Fig. 1. (a) Structure of $Ag_7O_8NO_3$ silver clathrate crystals that consist of a cubic lattice of Ag_6O_8 cages that enclose NO_3 anions. (b) SEM image of epitaxial (111)-oriented $Ag_7O_8NO_3$ platelets photodeposited on a TiO_2(110) substrate surface in a $AgNO_3$ solution at an electrode potential of +0.3V vs Ag.

formation can be obtained at a bias of +0.2V vs. Ag. The necessary photoexcitation was provided by a high-pressure mercury lamp at a flux of 28 mW/cm^2. X-ray diffraction analysis showed that the best orientation control could be achieved on TiO_2 (110) substrates, yielding micrometer-scale epitaxial platelets, shown in a scanning electron microscope image in Fig. 1(b). It is clear from the image that the platelets tend to assume a hexagonal shape, characteristic of (111)-oriented growth. The growth habit and epitaxial relationship were further studied by x-ray diffraction and epitaxial relationships were found.

The reason for the preferential formation of epitaxial clathrate crystals on TiO_2 (110) surfaces was analyzed in terms of lattice matching between the clathrate Ag_6O_8 cage pseudo lattice and the TiO_2 surface. The (110)-oriented TiO_2 surface has a tetragonal structure where the spacing between adjacent bridging oxygen rows is 6.495 Å. This distance matches reasonably well the clathrate cage spacings of 6.056 Å, when the clathrate lattice is viewed along the (111) direction. It appears that despite the 6% mismatch, an epitaxial relationship is formed during platelet growth. The growth mechanism is thus somewhat similar to the formation of C_{60} films on crystalline substrates, although the growth of a hexagonal (111)-oriented lattice on a tetragonal surface is unusual.

Various different anions can be integrated in the clathrate lattice. We compared the growth habit and growth rates of silver clathrates containing the HNO_3 and HSO_4 anions and found that while the growth rate of $Ag_7O_8HSO_4$ was much higher than for $Ag_7O_8NO_3$, the epitaxial relationship was weaker. Since the lattice parameter of the clathrates is predominantly set by the size of the Ag_6O_8 cages, it appears that the formation of large epitaxial platelets is limited by other factors, with variable anion incorporation kinetics in the Ag_6O_8 cages being the most likely reason. This work showed that epitaxial growth of inorganic cage compounds is possible when commensurate matching between the cage pseudo lattice and a single-crystal substrate occurs.

Reference
[1] R. Tanaka, R. Takahashi, S. Takata, M. Lippmaa, and Y. Matsumoto, CrystEngComm **17**, 3701 (2015).

Authors
R. Tanaka[a], R. Takahashi, S. Takata[a], M. Lippmaa, and Y. Matsumoto[a,b]
[a]Tokyo Institute of Technology
[b]Tohoku University

Vortices of Superfluid ^{3}He in a Narrow Cylinder

O. Ishikawa and T. Kunimatsu

Vortices are well known fluid phenomena, whose size is widely distributed from the scale of a galaxy to that of water vortices in a laundry machine. The vortices familiar to us are classical ones with circulating motion of fluid, which are well described by a classical fluid mechanics. In modern physics, other types of vortices are found in liquid ^{3}He and ^{4}He from a quantum mechanical point of view. Both of quantizing a circulation and having a localized vorticity characterize a vortex in superfluid. Especially superfluid
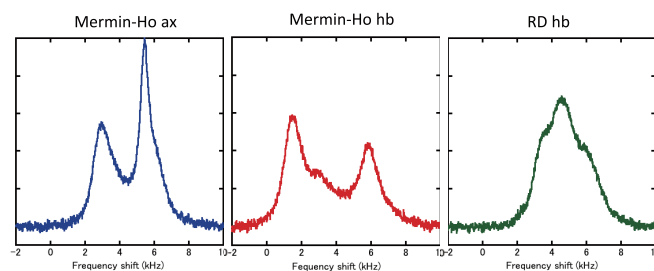

Fig. 1. Three types cw-NMR spectra in superfluid ^{3}He-A phase confined in a single narrow cylinder of 50 μm radius. Each spectrum corresponds to a different texture (spatial structure) of order parameters in the condensate.

^{3}He having many degrees of freedom in a condensate is more interesting than superfluid ^{4}He having only one type of vortex.

You can rotate normal liquid in a bucket by rotating the bucket itself but in the case of superfluid it is not easy to rotate it in such a way. Besides a vortex nucleation problem, stabilizing vortices in the bucket is another problem when the radius of bucket becomes very small, so-called a confined geometry. The necessary angular velocity of rotation to stabilize a vortex depends on the radius of cylinder and the quantity of circulation quantum of vortex. In superfluid ^{3}He-A phase, several types of vortex in bulk liquid have been observed but it was not clear whether another type vortex appears in the thin cylinder, where the angular velocity stabilizing a vortex becomes large. We showed that circulating velocity fields in superfluid ^{3}He–A phase were created in a very narrow cylinder, 100 μm in radius, using the rotating cryostat in ISSP, where three types of vortices were observed [1]. Two of three have the circulation quantum of unity and another had that of two, which was the same vortex as that in bulk liquid. Recently we can manipulate the type of vortex in even narrower cylinder, 50 μm in radius, in which three types of vortices are observed and all vortices correspond to the circulation quantum of unity [2]. A different type of vortex consists of different structures of order parameters of the condensate in a cylinder.

Figure 1 shows that three typical cw-NMR spectra in a single cylinder of 50 μm radius. A spectrum consists of a few spin wave resonances. Spin wave resonances are the low energy excitations in magnetic resonance experiments, whose frequencies are determined by NMR potential created by the dipole-dipole interaction E_D between ^{3}He nuclei in superfluid state. The order parameters in spin space and in orbital space are coupled each other through E_D. Three NMR spectra correspond to three types of textures, which are the spatial structures of order parameters in a cylinder. Our analysis reveals that they are Mermin-Ho hb texture, Mermin-Ho ax texture, and Radial-disgyration (RD) hb texture (see details in ref. [2]). These textures correspond to three types of vortices that can be observed in a narrow cylinder.

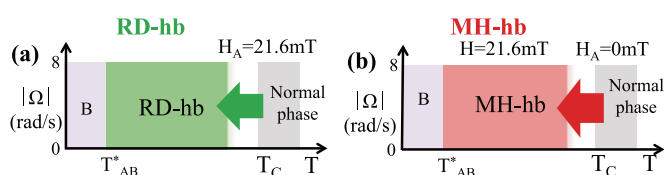We have always observed one of three NMR spectra and

Fig. 2. Stable textures on cooling under rotation at two kinds of magnetic fields. (a) RD hb texture appeared at 21.6 mT. (b) MH hb texture appeared at 21.6 mT after passing through Tc under 0 mT.

have not observed the spectrum where the textures coexist each other. Figure 2 shows the stability of textures in the rotation-temperature phase diagram strongly depends on the magnetic field on cooling through T_C (transition temperature between superfluid and normal fluid) under rotation. The experimental procedure is quite similar to that of field cooling technique in studies of superconducting material. Theoretical calculations have been done about the stability of texture under rotation in magnetic field [3]. There exist qualitative and quantitative discrepancies between calculated results and observed ones on the stability of the texture in varying temperatures, magnetic fields and rotation angular velocities. We think that these discrepancies are attributed to the metastable state of texture because the textural transition needs a higher energy state between textures.

References
[1] R. Ishiguro, O. Ishikawa, M. Yamashita, Y. Sasaki, K. Fukuda, M. Kubota, H. Ishimoto, R.E.Packard, T. Takagi, T. Ohmi, and M. Mizusaki, Phys. Rev. Lett. **93**, 125301 (2004).
[2] T. Kunimatsu, H. Nema, R. Ishiguro, M. Kubota, T. Takagi, Y. Sasaki, and O. Ishikawa, Phys. Rev. B **90**, 214525 (2014).
[3] Y. Tsutsumi and K. Machida, J. Phys. Soc. Jpn. **78**, 114606 (2009).

Authors
O. Ishikawa[a] and T. Kunimatsu[a]
[a]Osaka City University

Development of Metal Ion-Containing Ionic Liquid Catalyst on Mesoporous Silica

T. Sasaki

We have been developing and using metal ion-containing immobilized ionic liquid catalysts in order to design heterogeneous catalysts by utilizing the characteristics of ionic liquids, where ionic liquid molecule with imidazolium cation moiety is immobilized on silica support and the metal halogenate anions are introduced as counter anion serving as reaction centers [1, 2]. It was found that the ImmCu_IL containing $[CuCl_4]^{2-}$ is active for Kharasch addition reaction between styrene and CCl_4. ImmNi_IL was found to be active for Suzuki cross coupling reactions with chlroarenes and phenyl boronic acids. ImmPd_IL was found to be active in a phosphine-free condition for Suzuki cross coupling reaction for bromoarenes [2].

We report the synthesis and application of immobilized palladium metal-containing ionic liquid supported on mesoporous silica such as SBA-15 (ImmPd-IL@SBA-15) as a novel catalyst for organic reactions. There are several advantages by using mesoporous material such as SBA-15 as a support. It has high surface area, easy to prepare, high gas adsorption capacity and high temperature tolerance.
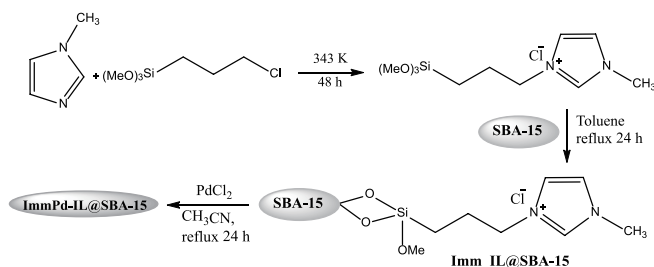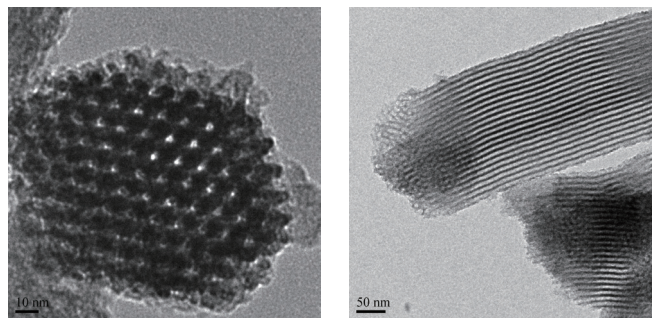

Fig. 1. TEM images of fresh ImmPd-IL@SBA15

The synthesis procedures were adopted from our method [1, 2] and all the reactions were conducted under nitrogen atmosphere (Scheme 1). Immobilized ionic liquid on SBA-15 samples were prepared using 1-methyl-3-(3-trimethoxysilylpropyl) imidazolium chloride (Mtim chloride). Mtim chloride was synthesized by refluxing the mixture of N-methylimidazole and 3-trimethoxysilylpropyl chloride at 70°C for 48 h. Mtim chloride and SBA-15 were dispersed in dehydrate toluene and refluxing, yielding solid products, Imm-IL@SBA-15. $PdCl_2$ and solid product were added to acetonitrile solution. After refluxing for 24 h, the resulting materials are obtained, denoted as ImmPd-IL@SBA-15. Fig. 1 shows TEM images for fresh ImmPd-IL@SBA15. Transmission Electron Microscope (JEOL JEM-2100 in ISSP, Univ. Tokyo) operating at 200 kV was used to obtain bright field images. It is found that uniform hexagonal channel structures are retained after immobilization of imidazolium groups. No Pd nanoparticles are found. The presence of $[PdCl_4]^{2-}$ was also confirmed by EDX analysis and EXAFS measurements.

It was found that the ImmPd-IL@SBA-15 catalyst has significantly improved the catalytic activity for synthesis of urea and oxamate derivatives by oxidative carbonylation of amines under co-catalyst, dehydrating agent and ligand free conditions [3]. ImmPd-IL@SBA-15 was also found to catalyze polyester amide synthesis by carbonylation polycondensation [4].

References
[1] T. Sasaki, C. Zhong, M. Tada, and Y. Iwasawa, Chem. Commun., 2506 (2005).
[2] T. Sasaki, M.Tada, C. Zhong, T. Kume, and Y. Iwasawa, J. Mol. Catal. A-Chem. **279**, 200 (2008).
[3] S. T. Gadge, E. N. Kusumawati, K. Harada, T. Sasaki, D. Nishio-Hamane, and B. M. Bhanage, J. Mol. Catal. A Chemical **400**, 170 (2015).
[4] A. Satapathy, S. T. Gadge, E. N. Kusumawati, K. Harada, T. Sasaki, D. Nishio-Hamane, and B. M. Bhanage, Catal. Lett. **145**, 824 (2015).

Authors
T. Sasaki[a], D. Nishio-Hamane, B. M. Bhanage[b]
[a]The University of Tokyo
[b]Institute of Chemical Technology

Scheme 1. Synthetic steps for the ImmPd-IL@SBA-15 catalyst.

Efficient Method for Membrane Protein Structure Predictions

Y. Okamoto

Membrane proteins have essential biological functions based on their structures for life, and atomistic structural information is important to investigate the mechanism of their functions. Computers have been developing for
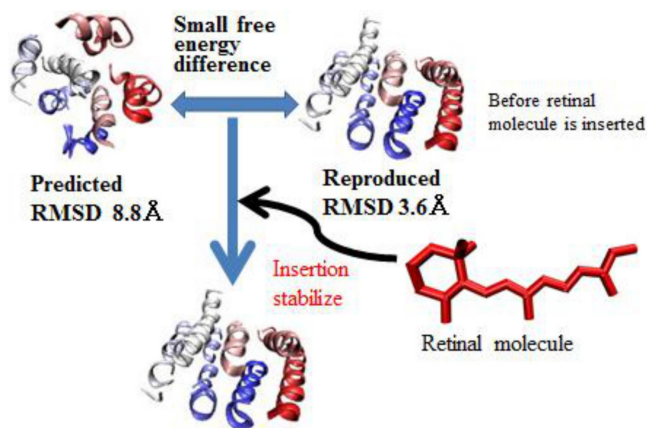
Fig. 1. Two predicted structures from our simulation and hypothesis about the relation between the structures and effects of retinal molecule insertion for the structures. In other words, the hypothesis is as follows: from our simulation without retinal molecule, the difference between above two structures is not large, however, insertion of retinal molecule into the empty space results in the stabilization of native-like structure compared to the other structure. This hypothesis is also consistent with previous experimental results.

decades. However, the resource runs short of structure predictions by brute-force simulations yet. Thus, efficient algorithm for computer simulation is needed to reduce computational resources for the prediction.

There are two fundamental approaches for the developments: decrease of interaction points in system and enhancement of sampling. A former example is to adopt an implicit solvent model. In good models, this method can achieve the structure prediction with simulations. A latter example is to employ replica- exchange method (REM) which enhances sampling of conformations. This method typically accelerates the crossing of free energy barriers using temperature change of replicas.

We developed the method from both approaches. We extended the previous method to target most membrane proteins [1]. Using the method, we performed structure prediction of bacteriorhodopsin and reproduced the native structure. Moreover, we also obtained the expected but unknown structure with empty space structure for retinal insertion, which is related to a hypothesis for co-molecule insertion during membrane protein folding as is shown in Fig. 1. As a result, our simulation produced the consistent results for previous experiments and supported the membrane protein folding hypothesis in co-molecule stage. Because we confirmed the validity of our new method for structure predictions, a next step will be to predict the unknown membrane protein structures or low-resolution protein structures.

We next proposed two new replica-exchange methods to increase efficiency of REM. One is the method of replica exchange with a differential equation without pseudo random numbers [2]. The other is the method that specifies the order of replica exchange and, thus, the trajectory in temperature space among replicas [3]. With 2-dimensional Ising model, we compared results of these new methods and its combination to results of the conventional Metropolis replica-exchange method. Figure 2 shows that specific heat obtained from the conventional Metropolis replica-exchange method (METREM), deterministic replica-exchange method (DETREM), designed-walk replica-exchange method (DEWREM), and their combination. DETREM with random-walk replica-exchange method reproduced the exact quantities including phase transition. Because short interval
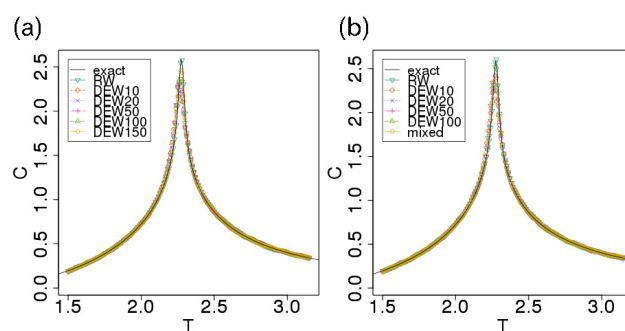

Fig. 2. Specific heat of 2-dimensional Ising model obtained by conventional random walk REM, DEWREM, and mixed simulations with (a) Metropolis replica-exchange method and (b) DETREM. The error bars are smaller than the symbols. In the inset, the labels are as follows. exact: exact solution, RW: random walk, DEWn: DEWREM with the interval of n MC steps between replica exchanges, and mixed: mixed walk.

causes correlation among replicas, DEWREM requires a longer interval of replica- exchange attempts to reproduce the conventional results. On the other hand, biomolecular simulation generally employs longer time interval between replica-exchange attempts. Hence, this does not cause such a problem in such simulations. In these simulations, DEWREM will result in the increase of efficiency of conformational sampling. For spin system, another implementation such as mixed walk simulation or different pairs in designed walk can improve the interval problem. These are future works to improve these methods.

References
[1] R. Urano, H. Kokubo, and Y. Okamoto, J. Phys. Soc. Jpn., in press.
[2] R. Urano and Y. Okamoto, arXiv:1412.6959.
[3] R. Urano and Y. Okamoto, arXiv:1501.00772.

Authors
R. Urano[a] and Y. Okamoto[a]
[a]Nagoya University

A New Structure Family of Oxide-Ion Conductor NdBaInO$_4$

M. Yashima and K. Fujii

Oxide-ion conducting materials such as pure oxide-ion conductors and mixed oxide ion-electronic conductors have a wide variety of applications in fuel cells, oxygen separation membranes and gas sensors. Since the oxide-ion conductivity is strongly dependent on the crystal structure, the discovery of new oxide-ion conductor belonging to a new structure family may open a new window for further innovative developments in the applications of oxide-ion conductors. Here, we report a new structure family of oxide-ion conductor NdBaInO$_4$ (Fig. 1) [1, 2].

To design a new layered perovskite-related structure, we have examined various chemical compositions of $AA'B$O$_4$ where A and A' are larger cations and B is smaller cation. After examining a number of chemical compositions, we discovered a new structure family of oxide-ion conducting materials NdBaInO$_4$ [1]. The Nd, Ba and In were chosen as cations, because (i) the different sizes of Nd and Ba can lead to the Ba/Nd cation ordering and (ii) the BaInO$_3$ perovskite layer can form from the view point of the sizes of Ba and In cations. Nd$_{1-x}$Sr$_x$BaInO$_{4-x/2}$ samples were prepared by solid-
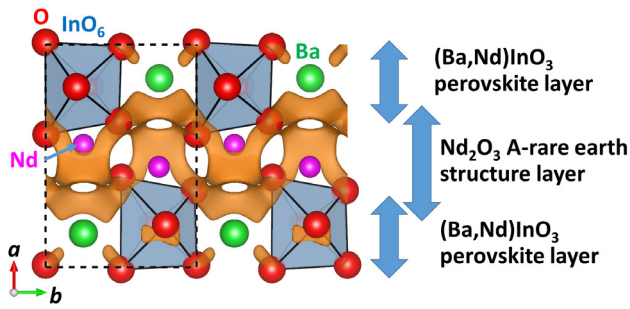
Fig. 1. Refined crystal structure and orange isosurface of the difference bond valence sum distribution for an oxide ion (O^{2-}) of $NdBaInO_4$. The structure consists of (i) Nd_2O_3 A-rare earth structure- and (ii) (Ba,Nd)InO_3 perovskite-layers. The difference bond valence sum map suggests that the oxide-ion conduction occurs in the Nd_2O_3 layer.

state reactions at 1400 °C using $BaCO_3$, $SrCO_3$, In_2O_3 and Nd_2O_3 powders. $NdBaInO_4$ and $Nd_{0.9}Sr_{0.1}BaInO_{3.95}$ exhibit oxide-ion conduction as shown in Figure 2. $NdBaInO_4$ and $Nd_{0.9}Sr_{0.1}BaInO_{3.95}$ samples are a single monoclinic phase with a new crystal structure as described below. Thus, a new structure family of oxide-ion conducting material $NdBaInO_4$ was discovered in this study. The oxide-ion conductivity of $NdBaInO_4$ is improved by Sr substitution at the Nd site (Fig. 2).

Crystal structure of $NdBaInO_4$ was investigated by neutron and synchrotron X-ray powder diffractometry and *ab initio* electronic calculations. We carried out the *ab initio* crystal structure analysis using the X-ray powder diffraction data. Neutron diffraction enables the precise determination of positional parameters of oxygen atoms. The space group was found to be monoclinic $P2_1/c$. The validity of the crystal structure of $NdBaInO_4$ (Figure 1) was confirmed by Rietveld refinements of synchrotron X-ray powder diffraction data measured at (i) SPring-8 and at (ii) PF, by Rietveld analysis of neutron diffraction data measured at (iii) J-PARC at (iv) ANSTO, and at (v) KAERI, (vi) by bond valence sums (BVS) of Nd, Ba and In atoms, and (vii) by the structural optimization based on the density functional theory (DFT) calculations. The refined crystal structure of $NdBaInO_4$ consists of (i) Nd_2O_3 A-rare earth structure- and (ii) (Ba,Nd) InO_3 perovskite-layers (Fig. 1), which indicates a new A/A' (Nd/Ba) cation ordered perovskite-related layered structure. An outstanding and unique feature of this new structure is that the edge of the InO_6 octahedron faces the A_2O_3 (Nd_2O_3) layer. The oxide-ion diffusion path of $NdBaInO_4$ was studied by the bond valence method (Fig. 1). The oxide ions can diffuse two-dimensionally in the A_2O_3 (Nd_2O_3) layer.
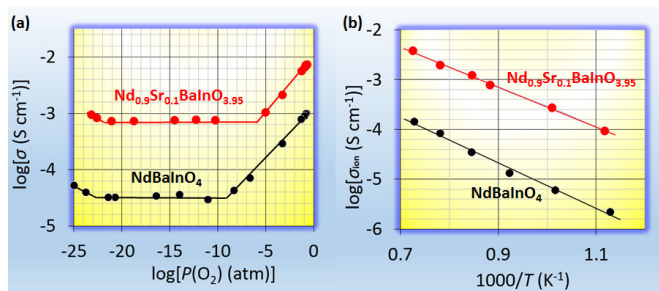

Fig. 2. (a) Oxygen partial pressure dependence of total electrical conductivity at 858 °C of $NdBaInO_4$ (Black) and $Nd_{0.9}Sr_{0.1}BaInO_{3.95}$ (Red). (b) Arrhenius plots of oxide-ion conductivity of $NdBaInO_4$ (Black) and $Nd_{0.9}Sr_{0.1}BaInO_{3.95}$ (Red).

References
[1] K. Fujii, Y. Esaki, K. Omoto, M. Yashima, A. Hoshikawa, T. Ishigaki, and H. R. Hester, Chem. Mater. **26**, 2488 (2014).
[2] K. Fujii, M. Shiraiwa, Y. Esaki, M. Yashima, S. J. Kim, and S. Lee, J. Mater. Chem. A **3**, 11985 (2015).

Authors
M. Yashima[a], K. Fujii[a], M. Shiraiwa[a], Y. Esaki[a], K. Omoto[a], A. Hoshi-kawa[b], T. Ishigaki[b], H. R. Hester[c], S. J. Kim[d], and S. Lee[d]
[a]Tokyo Institute of Technology
[b]Ibaraki University
[c]Australian Nuclear Science and Technology Organization
[d]Korea Atomic Energy Research Institute

Almost Perfect Frustration in the Dimer Magnet $Ba_2CoSi_2O_6Cl_2$

H. Tanaka and K. Kindo

Coupled spin dimer magnets provide a stage to embody the quantum physics of interacting lattice bosons. These magnets often exhibit a gapped singlet ground state. In an external magnetic field exceeding the energy gap, the $S_z = +1$ component of the spin triplet is created on the dimer. The $S_z = +1$ component, called a magnon, acts as a boson on the dimer lattice. The number of magnons can be tuned via the external magnetic field corresponding to the chemical potential. Magnons move to neighboring dimers and interact with one another owing to the transverse and longitudinal components of the interdimer exchange interactions, respectively. When the hopping term is dominant, magnons can undergo Bose–Einstein condensation while when the hopping term is suppressed so that the repulsive interac-
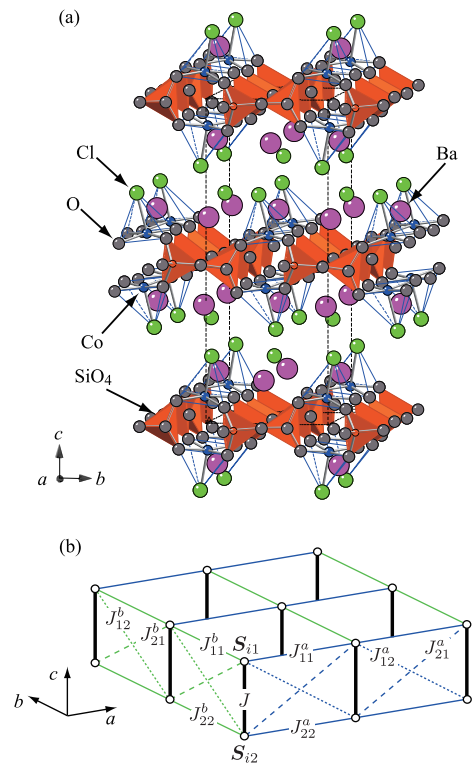

Fig. 1. (a) Perspective view of the crystal structure of $Ba_2CoSi_2O_6Cl_2$. Dotted lines denote the chemical unit cell. A magnetic Co^{2+} ion is located approximately at the center of the base of the CoO_4Cl pyramid, where the pyramids are linked via orange-colored SiO_4 tetrahedra in the *ab* plane. (b) Model of the exchange network for $Ba_2CoSi_2O_6Cl_2$. Thick solid lines represent the intradimer exchange interaction J, and thin solid, dashed and dotted lines represent the interdimer exchange interactions
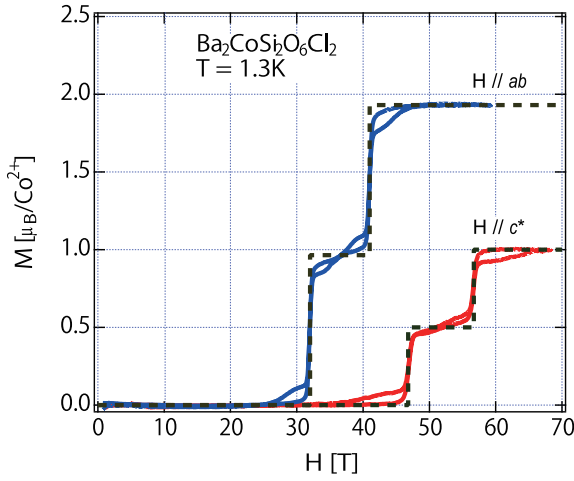
Fig. 2. Magnetization curves measured at 1.3K for $H \parallel c^*$ and $H \parallel ab$ using a piece of single crystal corrected for Van Vleck paramagnetism. Dashed lines are theoretical magnetization curves calculated using the anisotropy of the interdimer exchange interaction and the intradimer exchange interaction.

tion due to the antiferromagnetic interdimer interaction is dominant, magnons can crystallize to form a regular array.

Here we report the crystal structure of the spin dimer magnet $Ba_2CoSi_2O_6Cl_2$ and show that this compound exhibits magnon crystallization in a high magnetic field owing to the strong frustration of interdimer exchange interactions, which is different from the orthogonal dimer model [1]. The crystal structure consists of CoO_4Cl pyramids with a Cl^- ion at the apex, as shown in Fig 1(a). Magnetic Co^{2+} is located approximately at the center of the base composed of O^{2-}, which is approximately parallel to the ab-plane. Two CoO_4Cl pyramids form a chemical dimer with their bases facing each other. The magnetic property of Co^{2+} in an octahedral environment is determined by the lowest orbital triplet $^4T_1$. This orbital triplet splits into six Kramers doublets owing to spin–orbit coupling and the low-symmetric crystal field. When the temperature T is much lower than the magnitude of the spin–orbit coupling constant, the magnetic property is determined by the lowest Kramers doublet, and the effective magnetic moment of Co^{2+} is represented by the fictitious spin-1/2 operator [2, 3].

Figure 2 shows the magnetization curves for $Ba_2CoSi_2O_6Cl_2$ single crystal measured at 1.3 K for $H \parallel c^*$ and $H \parallel ab$. The entire magnetization process was observed up to a magnetic field of 70 T. The saturation of the Co^{2+} spin occurs at $H_s \simeq 57$ and 41 T for $H \parallel c^*$ and $H \parallel ab$, respectively. It can be clearly seen that the magnetization processes for both field directions are stepwise with a plateau at $M_s/2$. The singlet ground state is stabilized in a wide field range below H_c. These magnetization processes can be explained to consider that the interdimer exchange interactions are perfectly frustrated, which corresponds to the case $J_{11}^{ab} + J_{22}^{ab} = J_{12}^{ab} + J_{21}^{ab}$ within the exchange network shown in Fig. 1(b). In this case, the magnon cannot move onto the neighboring dimer, because the hopping amplitude is proportional to $J_{11}^{ab} + J_{22}^{ab} - J_{12}^{ab} - J_{21}^{ab}$. Hence, the ground state is determined by the balance between the Zeeman energy and the repulsive interaction between magnons. Consequently, a stepwise magnetization process with the $M_s/2$ plateau occurs, as observed in $Ba_2CoSi_2O_6Cl_2$.

In conclusion, this compound should be described as a 2D coupled spin dimer system with XY-like exchange interactions. $Ba_2CoSi_2O_6Cl_2$ exhibits a stepwise magnetization process with an $M_s/2$ plateau, irrespective of the magnetic

field directions. This finding shows that the frustration for the interdimer exchange interactions is almost perfect. The $M_s/2$ plateau state is almost exactly given by the alternate product of singlet and triplet dimers, which corresponds to a Wigner crystal of magnons.

References
[1] H. Tanaka, N. Kurita, M. Okada, E. Kunihiro, Y. Shirata, K. Fujii, H. Uekusa, A. Matsuo, K. Kindo, and H. Nojiri, J. Phys. Soc. Jpn. **83**, 103701 (2014).
[2] A. Abragam and M. H. L Pryce, Proc. R. Soc. London, Ser. A **206**, 173 (1951)
[3] M. E. Lines, Phys. Rev. **131**, 546 (1963)

Authors
H. Tanaka[a], N. Kurita[a], M. Okada[a], E. Kunihiro[a], Y. Shirata[a], K. Fujii[a], H. Uekusa[a], A. Matsuo, K. Kindo, and H. Nojiri[b]
[a]Tokyo Institute of Technology
[b]Tohoku University

Thermal Critical Properties of Two-Dimensional Generalized SU(N) Heisenberg Models

T. Suzuki, K. Harada, and H. Matsuo

In recent years, deconfined critical phenomena (DCP) [1] have attracted much attention in condensed matter physics. The transition that exhibits DCP is expected to take place between a magnetic ordered phase and valence bond solid (VBS) phase. The most famous model family that shows such phase transition is the two-dimensional Heisenberg models with multiple singlet-projection terms for SU(N) spins, namely SU(N) JQ_m models [2]. We investigated the quantum criticality between the Neel phase and the VBS phase in the JQ_2 model on the square lattice and the JQ_3 model on the honeycomb lattice by using quantum Monte Carlo (QMC) calculations [3]. From the finite-size scaling analysis, we found that data collapses for order parameters are obtained by the same scaling function independently of the lattice geometry. This result implies that the quantum phase transition in those models is of the second order transition. However, as the system size increases, the
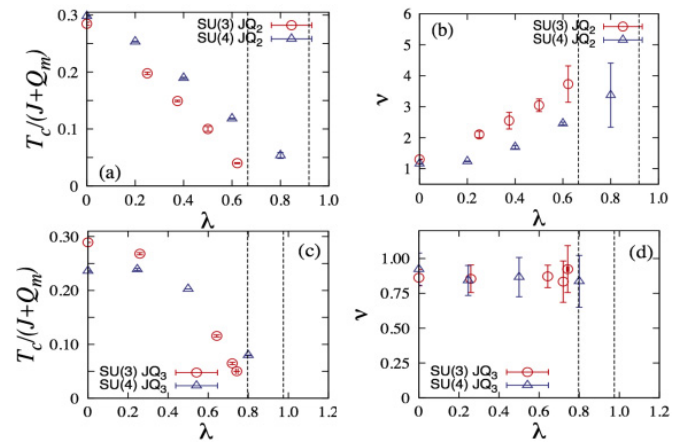

Fig. 1. Critical temperature T_c and critical exponent ν of the SU(N) generalized Heisenberg model. (a) and (c) ((b) and (d)) are results of T_c (ν) for the square-lattice and honeycomb-lattice case, respectively. Vertical dotted lines correspond to the quantum critical point between the Neel phase and VBS phase. The horizontal axis λ is the coupling ratio between Heisenberg interaction J and the amplitude of the multiple singlet-projection term Q_m, $\lambda = J/(J+Q_m)$.

estimated value of the quantum critical exponent ν exhibits a monotonic change and it approaches the phenomenological value for the first order transition. To discuss the quantum criticality from the different viewpoint and clarify the whole phase diagrams, we have studied the thermal critical properties of those models.

When we focus on the thermal properties of the SU(N) JQ_m models, the thermal phase transition to the VBS phase is possible because the VBS phase is characterized by coverings of the singlet dimers on the square or honeycomb lattice. We calculated the temperature dependence of the VBS order parameter by the QMC method. In figure 1, we show the critical temperature T_c and the thermal exponent ν which were evaluated from the finite-size scaling analysis up to L=192 for the square lattice case and L=96 for the honeycomb lattice case. Since the dimer covering state in the VBS phase is related to the rotational symmetry breaking of the lattice, we can expect the presence of the classical spin models that belong to the same universality class. In the present cases, the universality class of the square-lattice case is expected to be the same as that of the classical XY model with $\pi/2$-rotational symmetry breaking field, namely the XY+Z_4 model. In the honeycomb-lattice case, it may correspond to the three-state Potts model because the transition is characterized by $\pi/3$-rotational symmetry breaking. As shown in figure 1, ν increases monotonically in the square-lattice case when the system approaches the quantum critical point. It is obvious that the increase of ν survives in the vicinity of the quantum critical point. The similar behavior of ν is also observed when the classical XY+Z_4 model approaches the XY model limit, where the Kosterlitz-Thouless transition is realized. In the honeycomb lattice case, ν is almost constant at $\nu \sim 5/6$, the value of the three-state Potts universality class. If the system shows the first-order transition at a zero temperature, a shift of ν toward the first-order-transition value is expected in both cases. However, we found that the first-order transition is unlikely for $T_c/(J+Q_m) \gtrsim 1/100$.

References
[1] T. Senthil *et al*., Phys. Rev. B **70**, 144407 (2004); T. Senthil *et al*., Science **303**, 1490 (2004).
[2] A. Sandvik, Phys. Rev. Lett. **98**, 227202 (2007).
[3] K. Harada *et al*., Phys. Rev. B **88**, 220408 (2013).
[4] T. Suzuki *et al*., Phys. Rev. B **91**, 094414 (2015); J. Phy.:Conf. Series. **592**, 012114 (2015).

Authors
T. Suzuki[a], K. Harada[b], H. Matsuo[c], S. Todo[d], and N. Kawashima
[a]The University of Hyogo
[b]Kyoto University
[c]RIST
[d]The University of Tokyo